H-ABC– and dystonia-causing TUBB4A mutations show distinct pathogenic effects

Victor Krajka, Franca Vulinovic, Mariya Genova, Kerstin Tanzer, A. Jijumon, Satish Bodakuntla, Stephanie Tennstedt, Helge Mueller-Fielitz, Britta Meier, Carsten Janke, et al.

Victor Krajka, Franca Vulinovic, Mariya Genova, Kerstin Tanzer, A. Jijumon, et al.. H-ABC– and dystonia-causing TUBB4A mutations show distinct pathogenic effects. Science Advances , 2022, 8 (10), pp.eabj9229. 10.1126/sciadv.abj9229 . hal-03836008

HAL Id: hal-03836008
https://hal.science/hal-03836008v1

Submitted on 4 Sep 2024

CELLULAR NEUROSCIENCE

H-ABC– and dystonia-causing *TUBB4A* mutations show distinct pathogenic effects

Victor Krajka[1,8], Franca Vulinovic[1]†, Mariya Genova[2,3]†, Kerstin Tanzer[1], A. S. Jijumon[2,3], Satish Bodakuntla[2,3], Stephanie Tennstedt[4,5,6], Helge Mueller-Fielitz[7], Britta Meier[1], Carsten Janke[2,3], Christine Klein[1], Aleksandar Rakovic[1]*

Mutations in the brain-specific β-tubulin 4A (TUBB4A) gene cause a broad spectrum of diseases, ranging from dystonia (DYT-TUBB4A) to hypomyelination with atrophy of the basal ganglia and cerebellum (H-ABC). Currently, the mechanisms of how *TUBB4A* variants lead to this pleiotropic manifestation remain elusive. Here, we investigated whether *TUBB4A* mutations causing either DYT-TUBB4A (p.R2G and p.Q424H) or H-ABC (p.R2W and p.D249N) exhibit differential effects at the molecular and cellular levels. Using live-cell imaging of disease-relevant oligodendrocytes and total internal reflection fluorescence microscopy of whole-cell lysates, we observed divergent impact on microtubule polymerization and microtubule integration, partially reflecting the observed pleiotropy. Moreover, in silico simulations demonstrated that the mutants rarely adopted a straight heterodimer conformation in contrast to wild type. In conclusion, for most of the examined variants, we deciphered potential molecular disease mechanisms that may lead to the diverse clinical manifestations and phenotype severity across and within each TUBB4A-related disease.

INTRODUCTION

With progressively affordable methods for whole-genome sequencing, the number of known pleiotropic genes is steadily growing. Pleiotropy describes the phenomenon by which mutations in the same gene cause different clinical manifestations. For example, variants of *ATP1A3* are associated with alternating hemiplegia of childhood (*1*, *2*), rapid-onset dystonia-parkinsonism (*3*), and other distinct clinical manifestations (*4*, *5*). For most genes, the underlying mechanisms of genotype-phenotype relationships remain elusive. One of these genes is *TUBB4A*. In this study, we focused on mutations in β-tubulin 4A (TUBB4A), which are responsible for a broad phenotypic spectrum of movement disorders and more complex neurologic phenotypes.

Tubulins are the building blocks of the largest cytoskeletal filaments, the microtubules. Nine different α- and β-tubulin isoforms exist in humans, and their coding genes are differentially expressed throughout different tissues and cell types. Incorporating various tubulin isoforms is expected to influence the mechanical and dynamic properties of microtubules; however, only a few isotypes have been investigated in detail (*6*). Microtubules assemble spindles that segregate the sister chromatids during meiosis and mitosis; they serve as tracks for intracellular transport and act as a dynamic scaffold during migration and differentiation in all eukaryotic cells (*6*–*8*). In addition, microtubules are intrinsically dynamic because of the continuous insertion of α- and β-tubulin heterodimers—termed polymerization, punctuated by spontaneous collapses, denoted as "catastrophes," of the microtubule ends (*9*).

TUBB4A is predominantly expressed in the central nervous system. Brain regions with the highest expression levels are the white matter, the cerebellum, and the basal ganglia (*10*). Mutations in *TUBB4A* have been associated with isolated dystonia (DYT-TUBB4A) (*10*, *11*), isolated hypomyelination (*12*), and hypomyelination with atrophy of the basal ganglia and cerebellum (H-ABC) (*13*–*15*). The mild side of the phenotypic spectrum is represented by DYT-TUBB4A, characterized by the juvenile or adult onset of spastic "whispering" dysphonia and generalized dystonia (*16*, *17*). The severe end of the phenotypic spectrum is represented by H-ABC, first reported in 2002 (*18*). In contrast to DYT-TUBB4A, brain magnetic resonance imaging (MRI) scans of patients with H-ABC show white matter deterioration (*18*). The disease typically manifests within the first 2 years after birth; patients often have dystonia, nystagmus, and developmental delay, and as the disease progresses, they lose the ability to walk unaided (*13*, *14*).

However, the exact mechanisms underlying the pleiotropic effects of *TUBB4A* mutations remain elusive. So far, only a few mechanistic studies have been published. Three exclusively cell-based studies investigated the influence of disease-associated TUBB4A mutations on neurite outgrowth and microtubule dynamics (*19*–*21*). Nevertheless, the microtubule dynamics data were particularly contradictory across studies. Recently, rodent models for isolated hypomyelination and H-ABC were thoroughly characterized (*22*, *23*). The so-called *taiep* rat, which has a homozygous TUBB4A p.A302T mutation, presented solely glial impairment in the form of hypomyelination (*22*). In a mouse model with an H-ABC–linked TUBB4A p.D249N mutation, both neuronal and glial pathologies were detected, and altered microtubule dynamics were found in cortical neurons (*23*). However, to what extent TUBB4A mutations influence microtubule dynamics in disease-relevant oligodendrocytes has not been investigated to date. Additional DYT-TUBB4A cases were recently published, and for each TUBB4A variant, the potential impact on the protein structure was assessed using in silico modeling (*24*). Whether these structural

---

[1] Institute of Neurogenetics, University of Lübeck, Ratzeburger Allee 160, 23538 Lübeck, Germany. [2] Institut Curie, Université PSL, CNRS UMR3348, 91401 Orsay, France. [3] Université Paris-Saclay, CNRS UMR3348, 91401 Orsay, France. [4] Institute for Cardiogenetics, University of Lübeck, 23562 Lübeck, Germany. [5] DZHK (German Research Centre for Cardiovascular Research), partner site Hamburg/Lübeck/Kiel, 23562 Lübeck, Germany. [6] University Heart Center Lübeck, 23562 Lübeck, Germany. [7] Institute for Experimental and Clinical Pharmacology and Toxicology, University of Lübeck, Ratzeburger Allee 160, 23562 Lübeck, Germany. [8] Institute of Microtechnology (IMT), Technische Universität Braunschweig, Braunschweig 38124, Germany.
*Corresponding author. Email: aleksandar.rakovic@neuro.uni-luebeck.de

†These authors contributed equally to this work.

changes influence the molecular dynamics (MD) of the heterodimer remains to be investigated.

To understand the variable severity of clinical manifestations caused by different mutations in TUBB4A, we analyzed the effects of DYT-TUBB4A–causing mutations p.R2G and p.Q424H and H-ABC–causing mutations p.R2W and p.D249N on the microtubule network. The mutations were selected to represent two clinically distinct phenotypic presentations and to reflect different severities of the phenotype within each syndrome.

Two of the four investigated mutations (p.R2G and p.R2W) affect a highly conserved arginine in the N-terminal β-tubulin tetrapeptide Met-Arg-Glu-Ile (MREI). MREI is an autoregulatory domain that modulates the stability of tubulin mRNAs (*25*). The authors demonstrated that nonsynonymous p.R2 substitutions (including p.R2G and p.R2W) destabilize the autoregulation of β-tubulin mRNA, affecting the balance of β-tubulin subunits. The fact that the p.R2G and p.R2W mutations are located at the same site within the MREI domain and lead to two different disease expressions suggests that a mechanism other than tubulin mRNA stability may play an essential role in the development of DYT-TUBB4A and H-ABC.

We showed that all TUBB4A variants were integrated into the microtubules but to different degrees, reflecting the phenotypic severity. We also investigated the effect of TUBB4A mutations on the microtubule dynamics in vitro using total internal reflection (TIRF) microscopy. Microtubule growth speed, length, duration, and the number of growth events were differentially altered in H-ABC– and DYT-TUBB4A–causing mutants compared to wild type (WT). These microtubule properties were validated in primary oligodendrocytes. Last, all three intradimer mutations (p.R2G, p.R2W, and p.D249N) were modeled and simulated in silico, showing altered bending and twisting angle distributions compared to WT, suggesting a compromised degree of flexibility in the mutant heterodimers.

RESULTS

H-ABC– but not dystonia-linked TUBB4A mutants show impaired microtubule incorporation

To determine the functional consequences of dystonia- and H-ABC–associated mutations in TUBB4A, located at the intradimer site (p.R2G, p.R2W, and p.D249N) or the potential microtubule-associated proteins (MAPs) interaction surface (p.Q424H), we investigated their incorporation ability into the microtubules. To this end, we transduced U-2 OS cells with lentiviral particles expressing WT or mutant TUBB4A C-terminally tagged with green fluorescent protein (GFP) and investigated the degree of overlap (yellow) between total α-tubulin (inverted gray scale) and TUBB4A variants (inverted gray scale) (Fig. 1A). Cells solely expressing GFP served as incorporation negative control. Although the GFP signal was ubiquitously present in the negative control, the microtubule network (pan-α-tubulin) did not show a substantial colocalization with GFP. The overlap of both fluorophores could be enhanced because of increased cytosolic tubulin localization after cold shock–induced microtubule depolymerization (fig. S1). In contrast, all TUBB4A forms could integrate into the microtubules, represented by colocalized GFP-tagged tubulin and endogenous tubulin signals.

However, the H-ABC mutants displayed a more pronounced green background (similar to the GFP control) as compared to WT and other dystonia-associated mutants, hinting at the possibility that these particular mutants are incompletely incorporated into microtubules. Representative orthogonal views are shown in fig. S2. Notably, after cold shock treatment, the green shade was also observed in the other TUBB4A forms (figs. S1 and S2). To investigate whether the incomplete colocalization could be caused by differential expression or protein stability of GFP-tagged TUBB4A forms, we measured total α- and β-tubulin protein levels. Nevertheless, neither the GFP control nor the TUBB4A forms showed deregulated tubulin levels. We observed no differences in levels of GFP-tagged TUBB4A between the WT and mutant forms of TUBB4A although some TUBB4A mutations are positioned at the mRNA autoregulatory MREI domain (Fig. 1, B and C, and fig. S3). This observation indicated that H-ABC–associated TUBB4A mutants show a higher proportion of unpolymerized TUBB4A because of incomplete microtubule incorporation.

TUBB4A mutations show differential microtubule growth dynamics in vitro

To determine the reasons for the compromised microtubule incorporation of H-ABC–related mutants, we investigated microtubule polymerization in vitro. For this, we generated reporter plasmids coexpressing either WT or mutant TUBB4A together with end-binding protein 3 (EB3)–GFP to track growing microtubule ends in cells. The T2A self-cleavable site was introduced to separate TUBB4A from EB3-GFP (fig. S4A). Two days after the transfection of human embryonic kidney (HEK) 293T cells, we extracted, measured, and adjusted the total protein concentration. Only batches with comparable concentrations and EB3-GFP expression levels (verified under a fluorescence microscope) were used to perform TIRF microscopy (fig. S4B). Using microtubule guanylyl-(α,β)-methylene-diphosphonate (GMPCPP) seeds (red) as starting points, we monitored microtubule polymerization following the EB3-GFP signals over 400 s (Fig. 2A). After 30 s, H-ABC–associated mutants showed slower microtubule growth, shorter microtubules, and more frequent flickering of EB3-GFP signals compared to WT. The observed EB3-GFP flickering may indicate an intermittent stalling of microtubule polymerization. On the other hand, in one dystonia-associated mutant (p.Q424H), we observed a slightly faster growth rate and consequently longer microtubules relative to WT (Fig. 2A). We observed no substantial differences in any investigated parameters between p.R2G mutant and WT TUBB4A.

To quantify the microtubule growth dynamics, we generated kymographs by manually tracking microtubules (fig. S5). We assessed growth by calculating the following parameters: velocity, growth events per microtubule, run length, and run time. Consistent with previous findings, H-ABC mutants showed significantly lower microtubule growth velocities, more growth events per microtubule, and shorter run lengths and times compared to WT (Fig. 2, B to E). In contrast, the dystonia-linked p.Q424H mutant showed substantially higher velocities, fewer growth events per microtubule, and elevated run lengths and run times relative to WT. Again, the second dystonia-linked p.R2G mutant displayed no prominent differences to WT. The collected data lead to the notion that the H-ABC–associated TUBB4A variants (p.R2W and p.D249N) severely perturb microtubule polymerization. In contrast, the dystonia-related mutations showed either no impact on microtubule dynamics (p.R2G) or an even faster growth (p.Q424H) than WT.

In vitro analysis of microtubule dynamics reveals differential growth properties of TUBB4A mutants over time

After finding significant differences in microtubule growth parameters between TUBB4A mutants and WT, we investigated whether

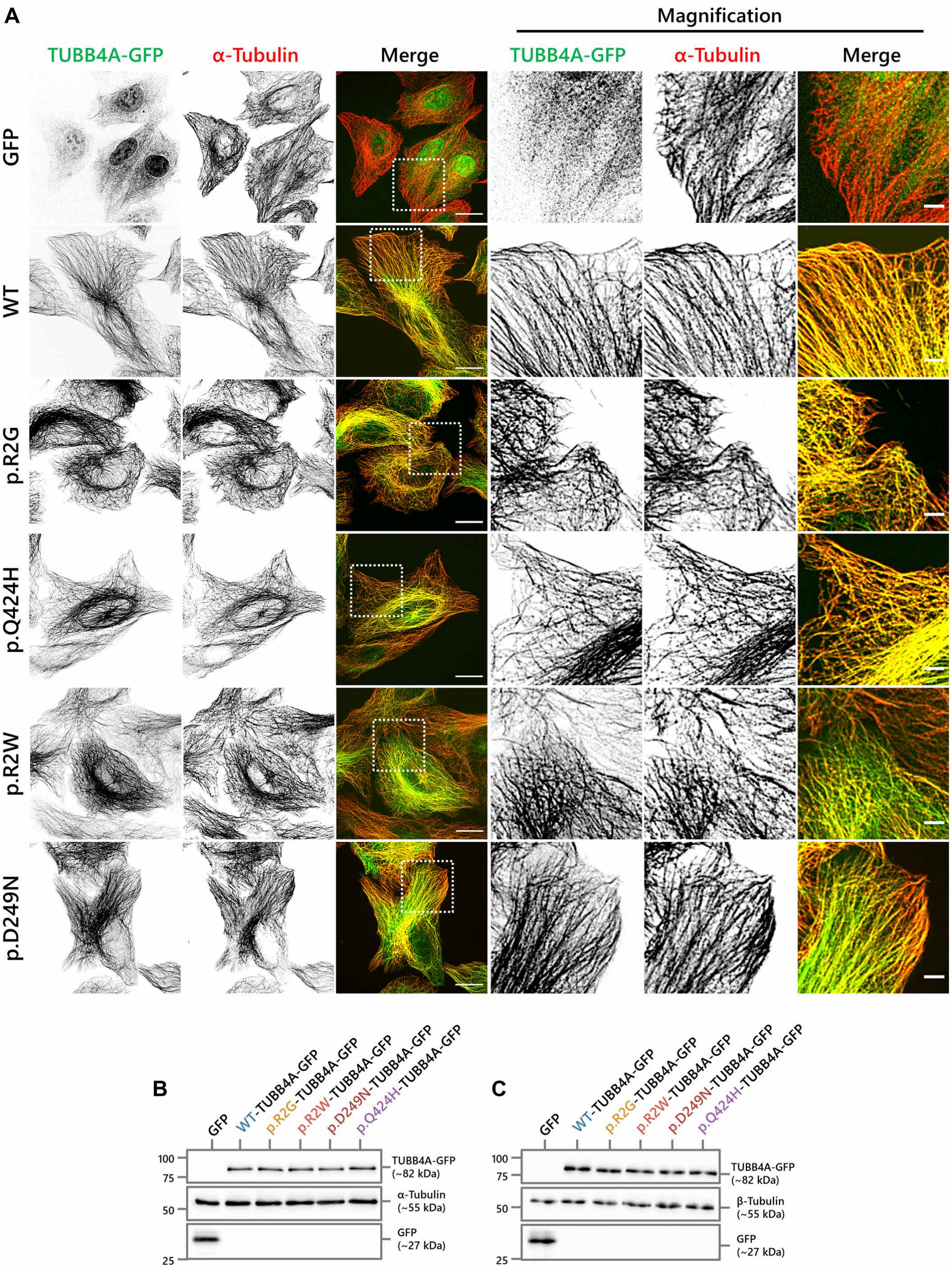

Fig. 1. Microtubule incorporation assay of GFP-tagged WT and mutant TUBB4A in U-2 OS cells. (**A**) Immunofluorescence staining of U-2 OS cells overexpressing either GFP or TUBB4A-GFP variants (inverted gray scale) against pan-α-tubulin (inverted gray scale). While the fluorescence signals of GFP and α-tubulin do not clearly overlap in the control, all TUBB4A forms show a prominent microtubule staining in both TUBB4A-GFP and α-tubulin channels and robust colocalization (merge, yellow). Scale bars, 20 and 5 μm (magnified panels). Immunoblots against TUBB4A-GFP and pan-α-tubulin (**B**) or pan-β-tubulin (**C**) show no alterations in tubulin composition or TUBB4A stability. Uncropped immunoblots are shown in fig. S3. In sum, H-ABC–linked but not dystonia-linked TUBB4A mutations show impaired microtubular integration.

microtubule dynamics change over time; as in some mutants, a different data dispersion emerged compared to WT. For example, both H-ABC–associated mutants (p.R2W and p.D249N) displayed a more dispersed data distribution for growth events (Fig. 2C), indicating a temporal change in the growth kinetics. For this, we averaged all measured data points per second for each growth parameter and plotted the mean values for every 30-s time window (fig. S6, A to D). The trend was determined via linear regression; the corresponding

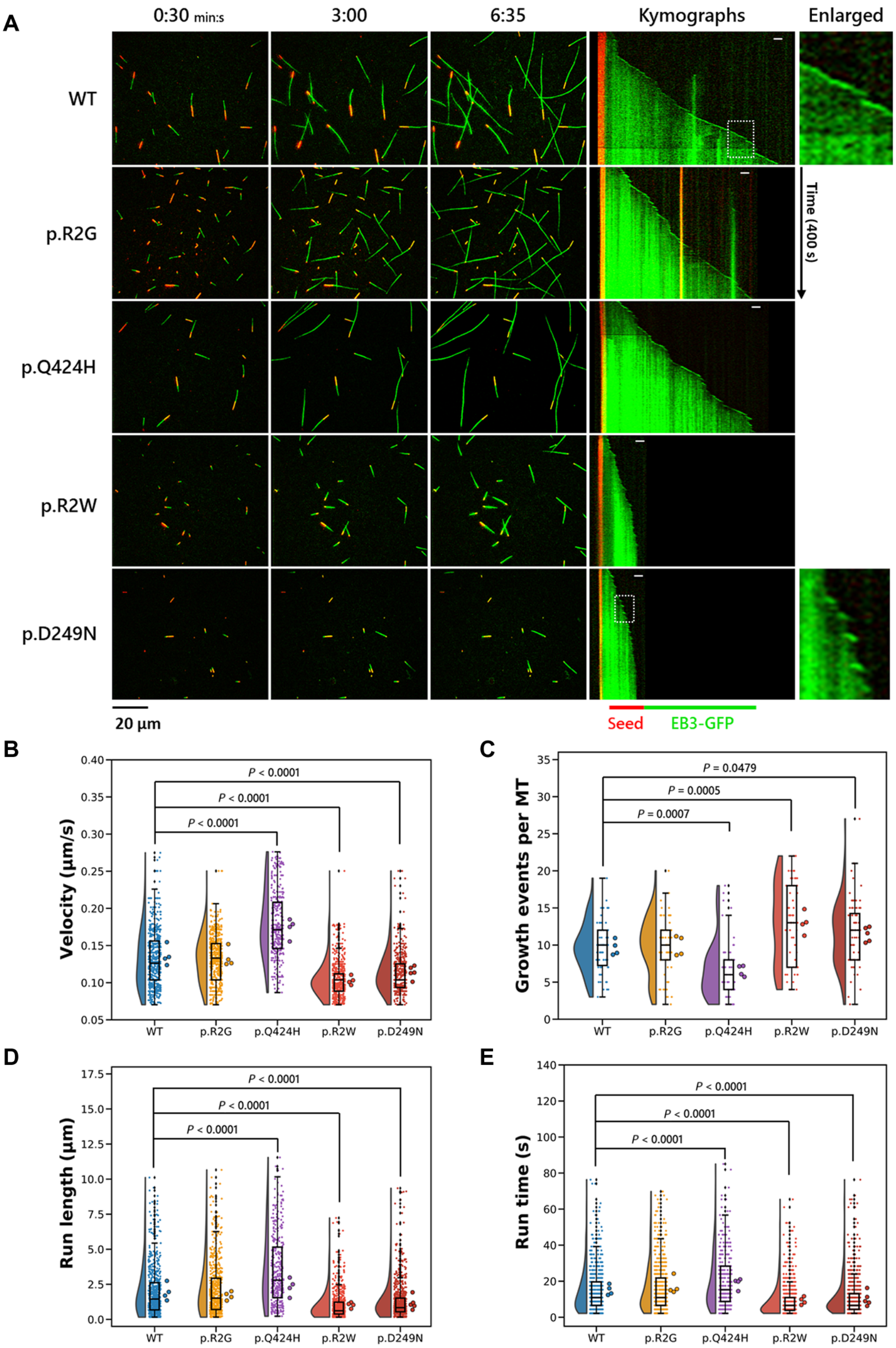

Fig. 2. Data distribution of microtubule growth parameters from whole-cell lysates containing WT or mutant TUBB4A. (**A**) TIRF microscopy time-lapse images at different time points (0:30, 3:00, and 6:35 min:s) of whole-cell lysates, showing EB3-GFP (green)–decorated growing microtubules from GMPCPP-stabilized and rhodamine-labeled seeds (red). Representative kymographs are shown to the right of the corresponding image sequences (white bars, 2 μm). (**B** to **E**) Data distribution and statistical analysis of EB3 comet (B) velocity, (C) growth events per microtubule, (D) run length, and (E) run time. Run length was defined as the microtubule growth distance between two pause events and run time as the growth duration between two pause events. The corresponding microtubule growth rate (velocity) was determined for each growth step. As growth event, every microtubule regrowth was counted [see enlargements in (A)]. The boxes show the quartiles of the dataset, the whiskers represent 1.5× of the interquartile range, the median values are indicated as horizontal lines inside the boxes, and data points outside the whiskers are marked as black diamonds. The mean values of the complete biological replicates are shown as filled circles on the right side of each boxplot. Statistical analysis of four to five independent experiments (transfection, cell culture, lysate preparation, and TIRF imaging) was applied by one-way analysis of variance (ANOVA) and post hoc Dunnett test. In total, 56 to 76 microtubules per TUBB4A form were analyzed. In sum, H-ABC–linked TUBB4A mutants display reduced microtubule growth in all parameters but elevated growth events, whereas p.Q424H led to faster and longer microtubule growth, with fewer growth interruptions. MT, microtubule.

regression line slopes are shown in bar plots on the right panel (fig. S6, A to D).

In comparison to WT, both H-ABC mutants displayed a significantly steeper decline in growth events per microtubule (fig. S6C). In contrast, the dystonia-linked p.Q424H mutant exhibited a significantly steeper decline in run length and run time (fig. S6, B and D) compared to WT. This confirms our assumption that the altered data distribution for some mutants is likely caused by changes in growth parameters over time.

In summary, we have seen that the H-ABC mutations displayed impaired microtubule incorporation and growth dynamics. We thus classify p.R2W and p.D249N as antimorphic mutations that affect microtubule polymerization as steric blocks (fig. S6F). In contrast, the p.Q424H mutant exhibited increased microtubule growth. Therefore, we categorize this TUBB4A variant as a gain-of-function mutation that enhances microtubule polymerization (fig. S6G).

Overexpression of disease-associated TUBB4A mutations in oligodendrocytes perturbs microtubule dynamics

Reduced white matter intensity due to a loss of oligodendrocytes is the pathological hallmark of H-ABC (*18*). Furthermore, transcriptomic analyses in both humans and mice revealed that *TUBB4A* expression increases with oligodendrocyte maturation (*26*–*28*). We thus investigated the impact of mutations in TUBB4A on microtubule dynamics and cellular morphology in mature oligodendrocytes. To this end, we isolated O4$^+$ cells from postnatal 7-day-old (P7) mice and transduced these cells with lentiviral particles expressing either WT or mutant TUBB4A-T2A-EB3-GFP (Fig. 3A). Four days upon transduction, soma and processes were analyzed using live-cell imaging (Fig. 3B and movies S1 and S2). In line with our TIRF microscopy findings, both H-ABC–associated mutants showed significantly stalled microtubule growth, shorter EB3-GFP comet lifetimes, and shorter run lengths in the soma and processes compared

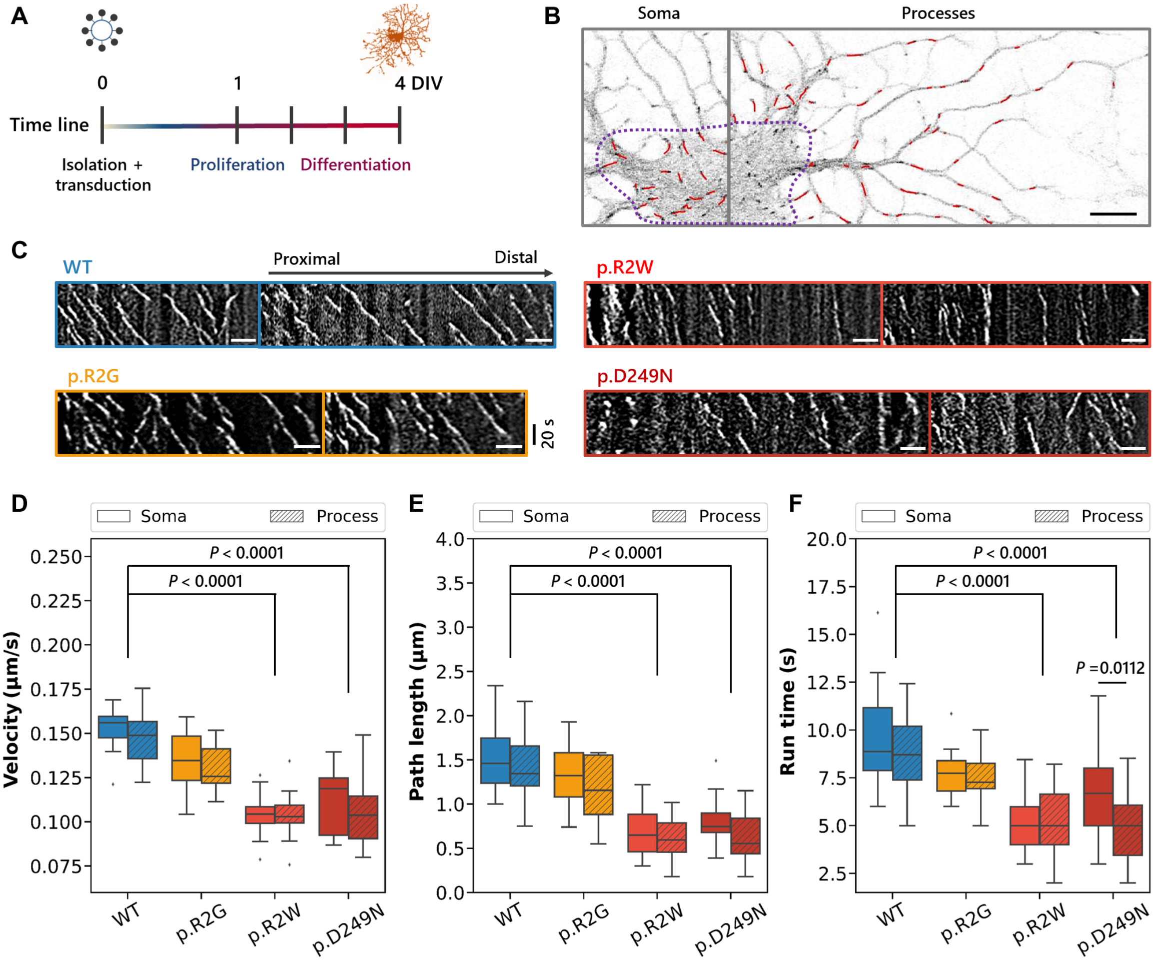

Fig. 3. Live-cell imaging of EB3-GFP comets in primary oligodendrocytes expressing either WT or mutant forms of TUBB4A. (**A**) Differentiation scheme for primary murine oligodendrocytes overexpressing WT or disease-causing TUBB4A mutations. (**B**) Example of tracked EB3 comets (red lines) in an oligodendrocyte either in the soma or along with processes. The region of interest (purple dotted line) either includes (soma) or excludes (processes) comet detection. Scale bar, 10 μm. (**C**) Representative kymographs display EB3-GFP comet trajectories for all TUBB4A forms in processes. Please note the declining comet speed at distal ends. Scale bars, 5 μm. Data distribution of microtubule growth velocity (**D**), EB3-GFP comet displacement (**E**), and run time (**F**). Data derived from the oligodendroctye processes are shown hatched. Statistical analysis: One-way ANOVA followed by Dunnett post hoc test; black horizontal lines inside each box indicate the median; whiskers represent 1.5× of the interquartile range. Outliers are visualized as black diamonds. Two independent experiments in total of 15 to 16 cells per TUBB4A variant. DIV, days in vitro. In sum, disease-causing TUBB4A mutations disrupt microtubule growth in oligodendrocytes in congruence with the severity of the corresponding disease phenotype.

to WT (Fig. 3, C to F). However, no significant differences in microtubule growth parameters were found between the dystonia mutant p.R2G and WT. In addition, for all TUBB4A forms, the mean growth parameters of the processes were nonsignificantly lower than from the soma and significantly different for the run time in the p.D249N mutant (Fig. 3F).

To determine whether altered microtubule dynamics influence oligodendrocyte morphology, we investigated cellular arborization using Sholl analysis. With this method, the ramifications were determined using concentric rings (fig. S7). Unexpectedly, we did not observe any morphological changes between O4$^+$ cells expressing either WT or mutant TUBB4A (fig. S7).

To investigate whether TUBB4A mutants are incorporated into the microtubule lattice, oligodendrocytes were transduced with lentiviral particles expressing GFP-tagged TUBB4A forms. For this purpose, we stained live cells with the oligodendrocyte marker O4 and subsequently with a secondary fluorescent antibody, and the microtubule marker SiR-tubulin (fig. S8). In line with previous observations, all TUBB4A variants colocalized with the microtubule lattice. Notably, compared to immunostained cells, the green background noise was detected in all TUBB4A forms. The enhanced cytosolic TUBB4A-GFP signal could result from longer acquisition times that typically occur during live-cell imaging. Overall, we demonstrated that the microtubule dynamics of all TUBB4A mutants were consistent compared to WT across the TIRF assays and in oligodendrocytes.

Protein integrity of α- and β-tubulin is not disturbed by disease-causing mutations located in the intradimer region

We further explored the impact of the disease-causing TUBB4A mutations on the heterodimer conformation by homology modeling and MD simulations (Fig. 4A). For this, we focused on p.R2G, p.R2W, and p.D249N mutations because they are located inside the intradimer region. To ensure that a biologically relevant heterodimer was modeled, we selected TUBA1A as α subunit and TUBB4A as β subunit. On the basis of previously published RNA sequencing datasets, both tubulins are highly coexpressed in human and murine oligodendrocytes compared to other α/β-isoforms (fig. S9) (*26*–*28*). Because no structure coordinates of a human TUBA1A/TUBB4A heterodimer were available, we chose a TUBA1B/TUBB2B heterodimer of a tubulin–stathmin–tubulin tyrosine ligase complex [Protein Data Bank (PDB) ID: 4IHJ (*29*)] with 97% identity between human TUBA1A and bovine TUBA1B and with 95% identity between human TUBB4A and bovine TUBB2B as a template for homology modeling. The query alignment is shown in fig. S10. After homology modeling, three additional heterodimers were generated, each containing one of the three TUBB4A mutations (p.R2G, p.R2W, and p.D249N) (Fig. 4A). The TUBB4A subunit ranged from p.M1 to p.A428 and TUBA1B

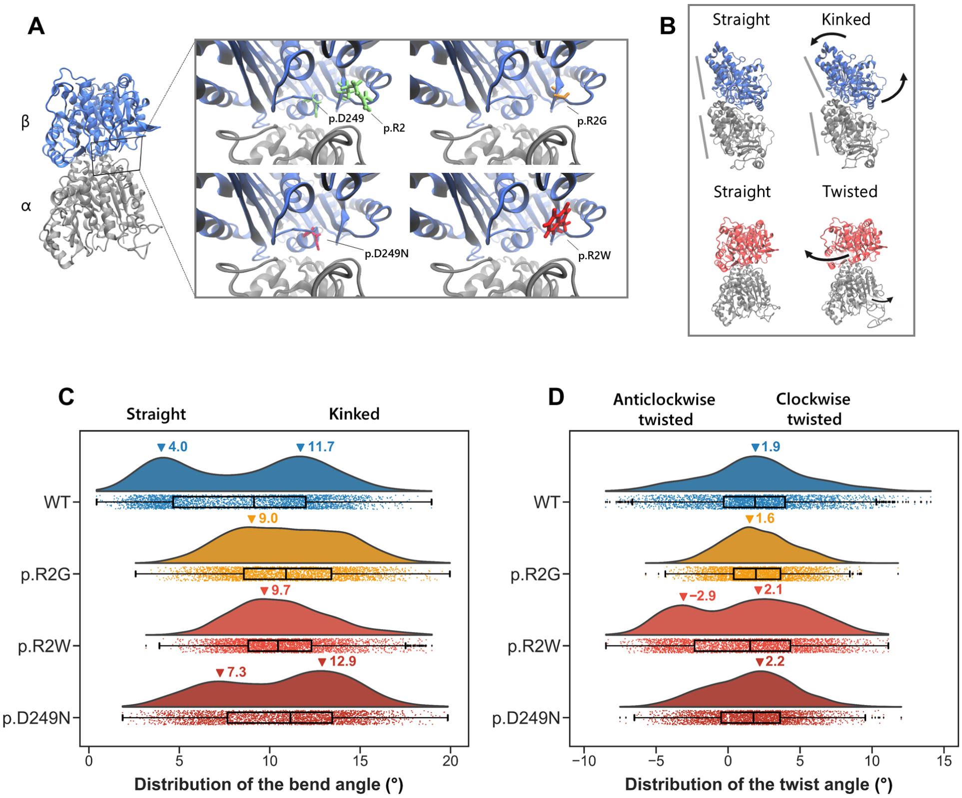

Fig. 4. In silico determination of tubulin heterodimer conformation. (**A**) Position of the modeled and simulated TUBB4A mutations in the intradimer region of a tubulin heterodimer. For better visualization, the nucleotides guanosine triphosphate and guanosine diphosphate are not shown. (**B**) Illustration of the main conformational changes of the heterodimer. (**C**) For the bending angle, the data distribution for WT and p.D294N is bimodal. For p.R2G and p.R2W, however, the data distribution is unimodal. Furthermore, all mutants show a right shift of the data compared to WT, which indicates that the mutant formed a rather curved heterodimer conformation. (**D**) The twist angle data distribution is unimodal for WT, p.R2G, and p.D294N, whereas it is bimodal for p.R2W. In sum, TUBB4A mutations located in the intradimer region cause differential bending and twisting conformations of the tubulin heterodimer.

from p.M1 to p.V434. Every heterodimer variant was subjected to three independent energy minimizations, followed by 1 μs of MD.

We first assessed the stability of each MD trajectory. For this, the root mean square deviation (RMSD) of the Cα coordinates was calculated to the reference structure (time point of 0 μs) for all systems. The RMSD values depicted that all systems reached an equilibrated state within the simulation time of approximately 50 ns. In addition, the single runs were comparable for each heterodimer variant (fig. S11, A to D). The structural fluctuation of the systems during their corresponding MD trajectories was determined by root mean square fluctuation (RMSF) (fig. S11, E and F). Fluctuations in the mutant systems were comparable to those in the WT system over most of the heterodimer structure. On the basis of the data, we did not find that the mutations affected the overall structure of the tubulin subunits as the total RMSD and RMSF levels were similar between WT and mutant systems.

Tubulin heterodimers containing H-ABC–linked TUBB4A mutations less frequently adopt a straight conformation compared to nonmutated heterodimers

Having determined that the disease-causing TUBB4A mutations do not perturb the overall structure of the tubulin subunits, we investigated whether they affect the MD of the heterodimer. We thus analyzed the main motion proportions using a principal components analysis (PCA). The resulting first four principal components (PCs) accounted for 61% WT, for 51% p.R2G, for 57% p.R2W, and for 56% p.D249N of the total variance (fig. S12). The WT heterodimer movement described by PC1 corresponds to a bending motion, accounting for 24% of the total variance (movie S3). Likewise, PC1 accounted for 22% of the p.R2G mutant variance, representing a bending motion. This means that the bending motion was the predominant conformal change for WT and the p.R2G variant during the MDs. In contrast, for the p.R2W heterodimer, PC1 represents a twisting motion, representing 30% of the overall movement. Furthermore, PC1 of the p.D249N heterodimer characterizes a movement in which the subunits show a bend-twist motion, representing 34% of the total variance. In short, this indicates an altered movement pattern in the H-ABC mutants compared to WT.

We further analyzed the angles for a bending and a twisting movement (Fig. 4B). For this, we applied a previously published script (*30*). The overall data distribution of both angles is considerably different for some mutants compared to WT (Fig. 4, C and D). In detail, the WT heterodimer showed a bimodal distribution of the curvature angle (Fig. 4C). This means that the WT heterodimer primarily adopted a straight (4°) and a curved (11.7°) conformation. On the other hand, a unimodal distribution is shown for p.R2G with a peak at 9.0° and for p.R2W at 9.7°. The data dispersion is wider (nearby uniform) for p.R2G, suggesting that the p.R2G-containing heterodimer is more flexible than the p.R2W counterpart, adopting various straight and bent conformations (Fig. 4C). In contrast, the p.D249N mutant has a bimodal distribution similar to WT but shifted to the right, with global maxima at 7.3° and 12.9°. In addition, a straight conformation occurred less frequently than a curved conformation. Therefore, the most notable finding is that the mutants have fewer low angular values than WT, indicating that the straight conformation is less frequently adopted. Besides, we observed that the WT TUBB4A–containing heterodimer straightened abruptly in two of three runs and remained in that position until the end of the simulation (fig. S13A). These sudden changes to a straight heterodimer conformation could not be detected in any mutants (fig. S13). Furthermore, the data distribution was also altered for the twisting angle for p.R2W compared to WT. While WT, p.R2G, and p.D249N have a unimodal value distribution, a bimodal distribution has been measured for p.R2W (Fig. 4D). Thus, the p.R2W mutant seems to adopt a second twisted conformation, which could not be detected for all other heterodimer variants. Together, for MD, both H-ABC mutants showed pronounced altered motions and conformations compared to WT, whereas the p.R2G mutant differed solely in the bending angle distribution.

Mutant heterodimers show distinct interaction clusters in the intradimer contact area compared to WT

Last, we investigated whether altered interactions within the intradimer region could account for the conformational changes. For this, we have clustered salt bridges (near the lumen, surface, and within the central intradimer interface) and hydrogen bonds (N terminus and central intradimer) according to their location in the heterodimer (Fig. 5, A and B) when positioned in a microtubule. By analyzing the MD trajectories of the WT heterodimer, we found that the interactions in the surface region occurred more frequently in a curved conformation. In contrast, the interactions in the lumen region were mainly formed in a straight conformation (Fig. 5C). Furthermore, interactions within the central intradimer were present almost throughout the entire trajectory.

Compared to WT, the p.R2G mutant showed a reduction of 13% in the luminal cluster (salt bridges) and the N terminus (hydrogen bonds) (Fig. 5, B and D). The other clusters displayed only minor differences in this mutant compared to WT. This indicates a general destabilization of the luminal/N-terminal intradimer region by the p.R2G mutation. In the p.R2W mutant, salt bridges were more frequently formed in the surface cluster (Fig. 5E). In the salt bridge abundance, the central intradimer and luminal clusters showed a reduction of 10 and 20%, respectively (Fig. 5B). Both hydrogen bond clusters were also reduced by 5 and 11%. Thus, the p.R2W mutation might lead to a more severe luminal and central intradimer destabilization compared to the p.R2G mutation. In contrast, in the p.D249N mutant, the binding frequency in both central intradimer clusters was increased by 15% (salt bridges) and by 17% (hydrogen bonds) (Fig. 5, B and F). In addition, this mutant showed the largest decrease in salt bridge frequency in the luminal cluster (40% versus WT) (Fig. 5, B and F). The p.D249N mutation seems to substantially stabilize the central intradimer region at the expense of luminal contact frequency. In summary, the mutations seem to cause a reduction (p.R2G) or a shift (p.R2W and p.D249N) in intradimer interactions. This could account for the reduced occurrence of a straight heterodimer conformation in the mutants compared to the WT.

DISCUSSION

The conundrum to be solved is how different TUBB4A mutations—some of which are located at the same position in the protein—can lead to a pleiotropic disease spectrum, ranging from dystonia with no signs of brain degeneration to H-ABC. In general, the manifesting phenotype seems to depend on the specific amino acid replacement and the respective position within the protein. In this study, we focused on TUBB4A mutations localized at either the lateral or longitudinal interaction sites. For TUBB4A in particular, mutations positioned within the (longitudinal) intra- and interdimer binding sites are usually more deleterious, leading to the complete clinical

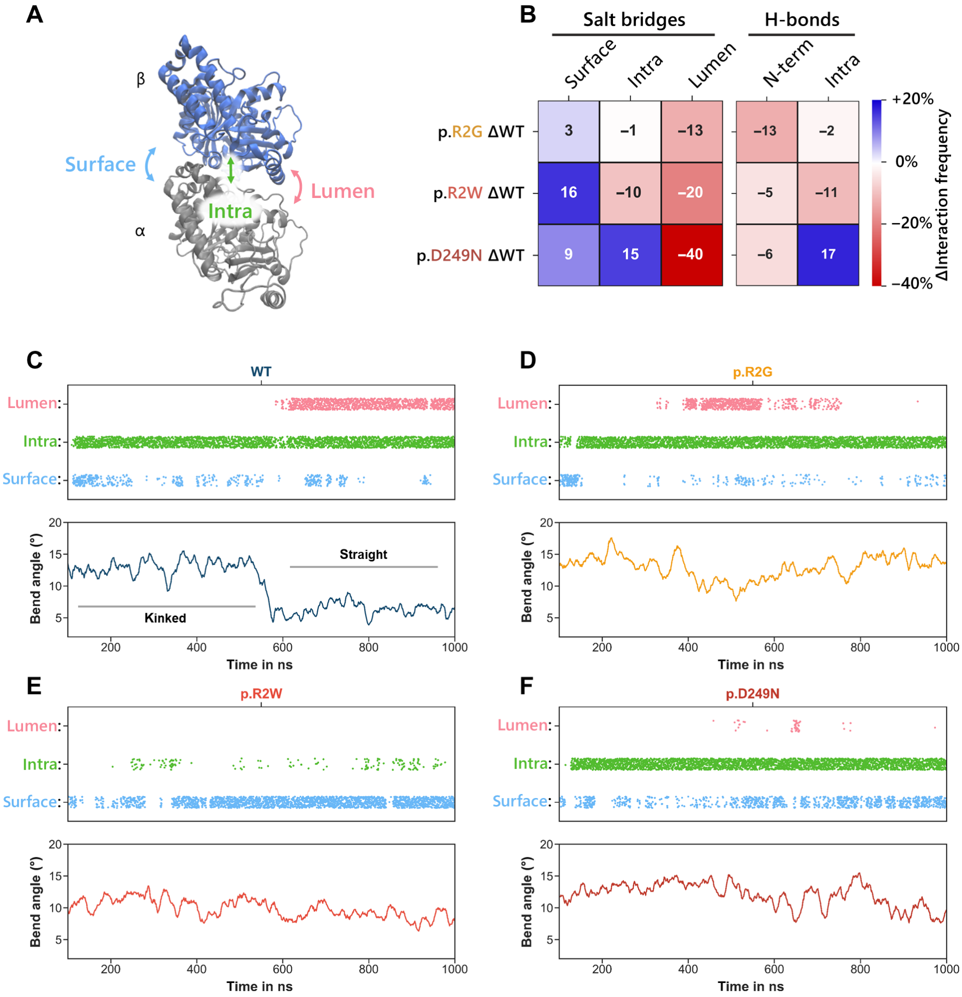

Fig. 5. Relative interaction frequency of salt bridges and hydrogen bonds within the intradimer contact site. (**A**) Schematic representation of interaction cluster positions in the heterodimer (side view). (**B**) Heatmap for salt bridges and hydrogen bond contact frequencies. Determining the relative salt bridge and hydrogen bond frequency revealed a destabilization in the luminal intradimer region in all mutants. The p.R2W mutant showed a stabilization in the surface cluster and a destabilization in the central intradimer (intra) cluster. In contrast, the p.D249N mutant displayed stabilization in the surface and intraclusters. (**C** to **F**) Occurrence of three salt bridges during conformal changes of the heterodimers. Salt bridges (TUBA1A:TUBB4A): lumen (p.R79:p.E45), central intradimer (p.E71:p.K252), and surface (p.K427:p.K401). In sum, the extent to which the luminal heterodimer interactions destabilize and the surface/central intradimer interactions stabilize is consistent with disease phenotype severity.

manifestation of H-ABC (*13*, *15*). As the predominant disease mechanism, mutations in the intradimer site could disturb microtubule integration (*31*). In contrast, mutations located at lateral sites (e.g., M-loop) or localized at possible MAP interaction sites tend to lead to less severe phenotypes, such as dystonia or isolated hypomyelination with or without atrophy of either the cerebellum or the basal ganglia (*11*, *12*, *15*, *24*). If the mutation is located on the outer surface of the microtubules, then increased microtubule growth could lead to this phenotype (*32*). Furthermore, the particular amino acid exchanged by the mutation can also affect the phenotypic appearance. For example, the mutation p.R2G leads to a form of dystonia, i.e., DYT-TUBB4A (*10*, *11*), whereas p.R2W and p.R2Q result in the development of severe H-ABC cases (*14*, *15*), although all three variants are located at the same position of the protein. These variants are situated within an N-terminal domain, autoregulating β-tubulin mRNA instability (*25*, *33*). In addition, even within the most severe phenotype (H-ABC), various distinct disease courses are observed, depending on the mutation (*14*, *15*, *34*, *35*). For instance, patients with p.R2W show, compared to p.D249N carriers, earlier first symptoms and reach fewer developmental milestones. To get an insight into whether these degrees of severity are reflected at the molecular level, we characterized the impact of the representative DYT-TUBB4A–causing mutations p.R2G and p.Q424H as well as the H-ABC–causing mutations p.R2W and p.D249N on microtubules in vitro.

We first examined their ability to incorporate into microtubules. This straightforward procedure is commonly used to gain a first insight into the mechanics of tubulin mutations (*31*, *36*–*38*). We demonstrated that all investigated TUBB4A mutations were incorporated into microtubules. However, H-ABC–associated mutants showed higher cytosolic localization of TUBB4A-GFP compared to other TUBB4A forms, indicating a higher amount of nonpolymerized TUBB4A-GFP. This observation could be reproduced in the other TUBB4A forms after cold shock treatment. Therefore, we suggest an antimorphic conformational change in the H-ABC mutants, but not to a complete loss of function of the affected tubulin heterodimers. Hence, the H-ABC mutants might act as steric hindrances during microtubule assembly.

Regarding mutations affecting the MREI domain, a previous study demonstrated a consistent decrease in mutant TUBB4A transcript levels in different cell types obtained from a patient harboring the p.R2G mutation (*11*), which is in contrast to earlier publications showing that mutations affecting arginine in MREI lead to increase in tubulin mRNA levels (*25*). This discrepancy could be partially explained by the difference in cellular models used in those studies, the differential behavior of overexpressed versus endogenously expressed mRNA, or tubulin isotype–specific properties.

Here, we observed no differences in overexpressed TUBB4A levels between WT and either p.R2G or p.R2W mutations, suggesting that the impaired autoregulation of TUBB4A mRNA does not play a major role in our cell model. This is consistent with the results of previous publications addressing mRNA and protein stability of TUBB4A (*19*, *20*). Notably, compared to other tubulin isoforms, TUBB4A does not appear to be susceptible to pharmacologically induced tubulin mRNA autoregulation (*39*). Alternatively, we propose that the disease-inducing effects of intradimer mutations are mainly caused by potential flexibility changes of the heterodimer rather than by deregulated mRNA stability.

To understand the effect of TUBB4A mutations on the heterodimer structure and MD, we have modeled and simulated the sterically adjacent intradimer mutations p.R2G (dystonia) as well as p.R2W and p.D249N (H-ABC) in silico. The dystonia-associated mutation p.R2G leads to an exchange of the positively charged arginine to the small amino acid glycine, while in p.R2W, the same amino acid is exchanged to a bulky, sterically confined tryptophan. In p.D249N, a negatively charged aspartic acid is replaced by a polar, uncharged asparagine. None of the mutations has altered the globular tubulin structure. Notably, all three mutants showed altered bending angle distributions compared to WT. The less frequently adopted straight conformation in the mutant systems could be explained by the reduced formation of luminal salt bridges. Furthermore, both H-ABC mutations seem to have rearrangements in the intradimeric contact area, which might stabilize the open conformation. Concerning the twisting angle, only the p.R2W mutant showed a different bimodal angle distribution compared to the other TUBB4A forms. In conclusion, regarding the MD, the H-ABC mutants displayed more pronounced differences in the motion and angle analysis to WT than the p.R2G mutant. The assumed antimorphic effect of the H-ABC mutants could be explained by the reduced probability of adopting a straight conformation. Thus, these mutant heterodimers could act as steric blocks during microtubule assembly. Nevertheless, disease severity may also be influenced by other heterodimer properties not studied here, such as lateral interactions with MAPs.

Furthermore, we investigated the impact of TUBB4A variants on microtubule dynamics using TIRF microscopy and live-cell imaging in primary oligodendrocytes. In line with the microtubule incorporation data, mutant tubulins affected the microtubule dynamics. When compared to WT TUBB4A, the dystonia-associated mutants showed either no differences (p.R2G) or considerably increased growth dynamics (p.Q424H). On the other side of the phenotypic spectrum, the H-ABC–causing mutations p.R2W and p.D249N showed significantly reduced growth dynamics. This underscores our assumption that the H-ABC mutations have a sterically unfavorable effect on the heterodimers. One possible reason could be altered heterodimer flexibility. This flexibility seems necessary for tubulin heterodimers because they have to undergo a conformational transition from a curved to a straightened state during microtubule assembly (Fig. 6, A to D) (*40*). Using p.Q424H, we characterized a recently reported TUBB4A mutation, leading to a very severe form of dystonia (*24*). We hypothesized a different disease-causing mechanism for this mutation than for the intradimer mutations because it is located on the microtubules' outer side, potentially affecting MAP interactions (see kinesin motor interaction with tubulin heterodimer; PDB code: 4LNU) (*41*). Our findings are consistent with previous studies showing that tubulin mutations proximal to p.Q424H lead to either longer neurites or more stable or faster-growing microtubules (*32*, *42*), indicating a gain-of-function mechanism.

We showed that the mutants exhibited differential microtubule growth characteristics over time using our microtubule dynamics analysis approach. For example, we observed that the number of growth events decreased substantially in the H-ABC mutants compared to WT. The initially high number of growth events indicates very frequent growth pauses, possibly induced by defective incorporation of the antimorphic heterodimers. This is in line with the observed frequent EB3-GFP flickering. The sterically unfavorable heterodimers potentially accumulate over time in the nonpolymerized tubulin pool, as unmutated tubulin might be incorporated more frequently than mutated. In parallel, because of this "sorting effect," the total amount of incorporation-competent tubulin might decrease. This assumption could explain the steep decline in growth events and general lower growth parameters, as the accumulation of nonpolymerized mutant heterodimers could compromise microtubule assembly even more. In contrast, the p.Q424H mutant showed significant reductions in run length and run time, although the initial values were higher compared to WT. This mutation might enhance microtubule growth through a gain-of-function mechanism, resulting in faster incorporation of nonmutated and mutated heterodimers. Over time, the nonpolymerized tubulin pool decreases, leading to a faster growth decline. This corresponds with significantly fewer growth events than WT due to longer growth phases, which were less often interrupted.

On the methodological aspects of the TIRF experiments, we are aware that the high EB3-GFP concentration, which leads to a complete microtubule EB3-GFP decoration, could mask the impact of mutations with mild effect on microtubule dynamics. Nevertheless, we did not observe any significant differences between WT and p.R2G using live-cell recordings, although the EB3-GFP decoration was present at the microtubule plus-end tips only. Furthermore, our observed WT TUBB4A EB3-GFP velocity data [4 days in vitro (DIV)] are consistent with a recent publication analyzing microtubule growth at various time points of oligodendrocyte differentiation (*43*). In our case, the shorter microtubule growth intervals could be caused by faster recording rates or based on divergent analysis methods. Consistent with recent data on microtubule growth in neurons, the measured EB3-GFP velocity and displacement length decreased with increasing distance to the soma (*44*). Microtubule growth rates are not constant during oligodendrocyte development (*43*). However, the effect of altered microtubule dynamics on oligodendrocyte differentiation remains to be elucidated.

Notably, we did not observe any evident morphological perturbations in primary oligodendrocytes (DIV4) expressing either of the TUBB4A mutants [in contrast to a recent H-ABC mouse model (*23*)]. However, we detected altered microtubule dynamics. Thus, morphological changes might occur at later differentiation stages.

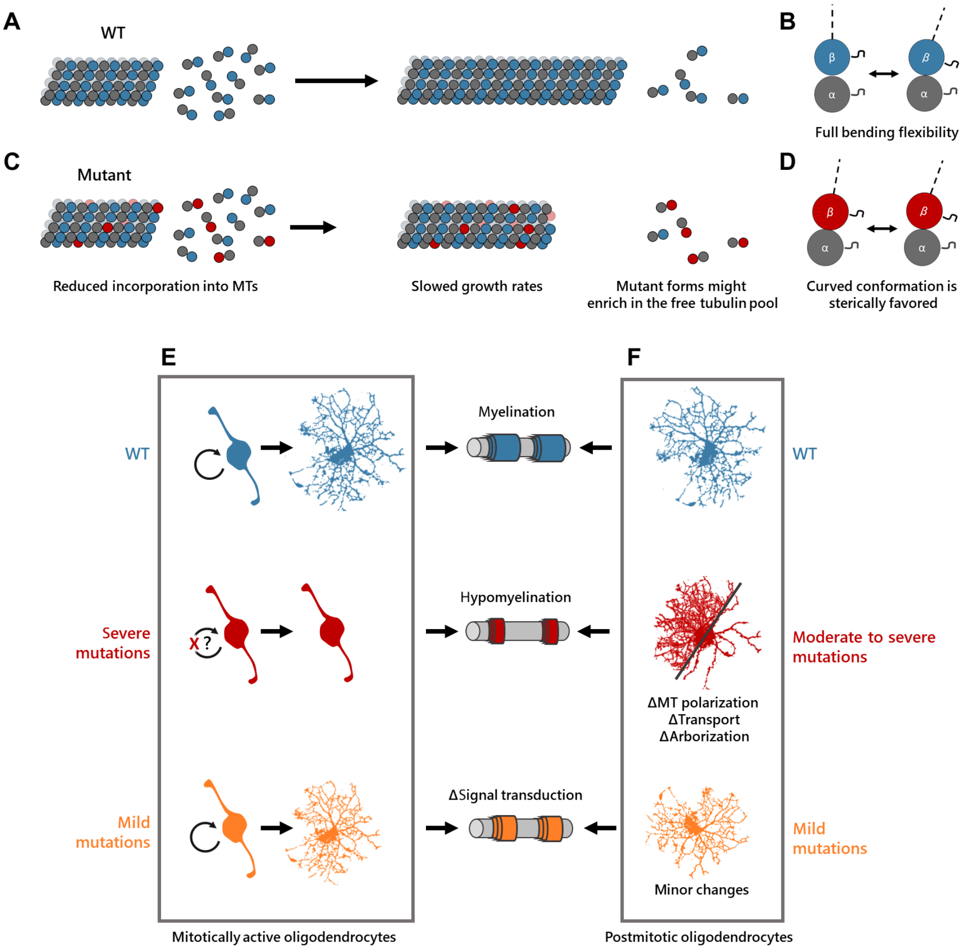

Fig. 6. Interpretation of the observed effects of TUBB4A mutants on microtubular dynamics, heterodimer flexibility, and oligodendrocytic fate. (**A**) WT TUBB4A can incorporate into microtubules, leading to elongation. (**B**) MD analysis showed that the WT heterodimer adopts a range of straight and curved conformations. (**C**) H-ABC–causing mutants demonstrated reduced incorporation into microtubules and slower growth. Because of the changes in microtubule dynamics over time, it is tempting to speculate that the mutants accumulate in the free tubulin pool. Ultimately, although similar tubulin concentrations could be present compared to WT, the amount of incorporable tubulin might be reduced, slowing microtubule growth. (**D**) The in silico simulation of intradimer mutations revealed that the straight conformation is less likely adopted, possibly leading to sterical hindrances during microtubule polymerization. (**E**) We hypothesize that TUBB4A mutations severely affecting microtubule dynamics disrupt proliferating oligodendrocytes. This results in fewer myelin-forming cells, leading to hypomyelination shortly after birth. (**F**) Moderate to severe TUBB4A mutations presumably enable the formation of myelinating oligodendrocytes. However, the myelination efficiency is markedly reduced because of microtubule alterations, displayed by hypomyelination at subtle later time points. In contrast, dystonia-related TUBB4A mutations might only lead to minor changes within oligodendrocytes, putatively resulting in altered signal transduction, while MRI scans of the brain show no apparent loss of white matter.

This is consistent with a recent pharmacological study in which primary postmitotic oligodendrocytes (DIV3 to DIV10) were treated with microtubule stability–modulating agents at sublethal concentrations (*45*). Microtubule polymerization inhibitors (nocodazole and vincristine) resulted in a relative increase in both branching and myelin basic protein (MBP)–positive areas. Vice versa, decreased MBP-positive area and total branching length were observed after microtubule stabilization (Taxol and epothilone). Notably, both treatment types significantly reduced myelin sheath wrapping events along with neuronal extensions. On the basis of our study and the data from recent publications, two main disease mechanisms for TUBB4A-related conditions can be extrapolated, which eventually converge on hypomyelination.

The first one mainly involves precursor-stage oligodendrocytes (Fig. 6E). In this mitosis-intensive developmental phase, the TUBB4A expression level increases markedly. Therefore, strong microtubule-destabilizing TUBB4A mutations (e.g., p.R2W and p.D249N) could significantly impair cell division, which might be less affected by polymerization-promoting mutations (e.g., p.Q424H). This assumption is in line with pharmacological studies in which microtubule-destabilizing versus microtubule-stabilizing reagents seem more toxic for frequently dividing cells (*46*). Therefore, too few mature oligodendrocytes might be formed, resulting in hypomyelination (*23*). Recently, a zebrafish model showed that most oligodendrocytes undergo cell division directly before final maturation (*47*). Therefore, future studies should focus on the effects of TUBB4A mutations on proliferative oligodendrocyte progenitor cells. To our knowledge, the influence of TUBB4A mutations on the mitotic spindle apparatus is still unknown.

The second proposed pathomechanism affects postmitotic oligodendrocytes (Fig. 6F). A certain percentage of progenitor cells that can divide despite moderate to strong TUBB4A mutations allow the differentiation into mature oligodendrocytes. However, subsequent arborization and myelination might be disturbed. This could be demonstrated in two rodent models in which uniform microtubule polarity was presumably disrupted in oligodendrocytes. In the so-called *taiep* rat, a p.A302T TUBB4A mutation might lead to impaired intracellular transport (*22*). In particular, the retrograde dynein-mediated mRNA transport seems elevated (*48*). A similar phenotype is seen in a microtubule organization–deficient TPPP^{KO} rat model (*43*). In this model, fewer microtubules nucleate from Golgi outposts, leading to disruptive microtubule polarization and excessive proximal extensions. In addition, while myelin sheath connections appear normal in these mutants, the individual myelin segments are significantly shorter, suggesting, as in the *taiep* model, a defective intracellular transport–induced hypomyelination.

In the case of dystonia-associated mutations, the second proposed pathomechanism might be mainly disease-causing (Fig. 6F). Arborization and myelination could be impaired sufficiently to affect signal transduction, although, in contrast to H-ABC, too mild to promote substantial atrophy. This assumption is consistent with the much later mean age at onset of TUBB4A-DYT compared to H-ABC. This threshold discriminating between cell death and defective signal transduction might explain the pleiotropic clinical pictures of TUBB4A-related diseases.

Together, our results suggest that the expressivity of the TUBB4A mutation–caused clinical manifestations is dependent on the overall impact of the mutations on microtubule dynamics. The TUBB4A mutations that we analyzed here have differential effects at the cellular and molecular levels that correspond to the type and severity of clinical phenotypes. When a certain molecular threshold is exceeded (resulting from the expression levels and the type of mutation), the effect of altered microtubule dynamics might be severe enough to influence cellular functions, e.g., mitosis or cell migration. If the altered microtubule dynamics can be compensated for during early development, then the phenotype might manifest as a long-term effect at later time points on other cellular functions, e.g., intracellular transport or signal transduction.

MATERIALS AND METHODS

Plasmid construction and mutagenesis

Plasmids (pER4) expressing GFP-tagged TUBB4A variants and EB3-GFP were previously described (*20*). For our recent study, we have modified the plasmids to either tag TUBB4A variants C-terminally with GFP or coexpress with EB3-GFP. For the former, the fragment encoding for a FLAG-tag was removed and replaced by GFP (pER4-TUBB4A-Linker-GFP). For the latter, WT TUBB4A with an N-terminal T2A self-cleavage peptide sequence was inserted upstream of EB3-GFP (pER4-TUBB4A-T2A-EB3-GFP). The cleavage efficiency was confirmed by immunoblotting. Subsequently, the following TUBB4A mutations c.4C>G (p.R2G), c.4C>T (p.R2W), c.745G>A (p.D249N), and c.1272G>C (p.Q424H) were generated using the QuikChange II site-directed mutagenesis kit (Agilent, Santa Clara, CA, USA) according to the manufacturer's protocol.

Lentiviral particle production for U-2 OS cells

For lentivirus production, Lenti-X 293T cells (Takara) were seeded at a density of 0.45×10^6 cells per well of a six-well plate and transfected on the following day with a transfection mix containing 1.6 μg of pTRIP GFP control plasmid or pER4 vector with TUBB4A-GFP variant of interest, 1 μg of psPAX2 (a gift from D. Trono; Addgene, plasmid #12260), 0.4 μg of pCMV-VSVG (a gift from B. Weinberg; Addgene, plasmid #8454), 8 μl of TransIT-293 (Mirus Bio LLC), and 200 μl of serum-free Dulbecco's modified Eagle's medium (DMEM) (Gibco). The next day, the medium was changed to 1.5 ml per well of serum-free minimum essential medium (MEM) (Gibco). The virus-containing medium was collected 32 hours later, cleared through a 0.45-μm syringe filter, and 400 μl per well was directly used to infect U-2 OS cells, seeded at low confluency on 24-well plates and 12 mm round coverslips.

Immunocytochemistry of U-2 OS cells

U-2 OS cells seeded on 12 mm round coverslips and infected with GFP control or TUBB4A-GFP variants were fixed with 4% paraformaldehyde 48 hours after viral infection, using a previously described protocol that allows for better preservation of the microtubule network (*49*). Fixed cells were blocked with 10% horse serum in phosphate-buffered saline (PBS) for 30 min at room temperature. Afterward, the samples were incubated with a monoclonal antibody against α-tubulin (1:2000 dilution; clone DM1A, Sigma-Aldrich) in PBS containing 0.1% Triton X-100 and 3% bovine serum albumin for 2 hours at room temperature. The fixed cells were subsequently washed three times with PBS–0.1% Triton X-100 and incubated with a secondary antibody (1:500 dilution; Alexa Fluor 647–conjugated goat anti-mouse, Invitrogen) and 4′,6-diamidino-2-phenylindole (1 μg/ml) for 1 hour at room temperature. Following three final washes, the cells were mounted on microscopy slides using the ProLong Gold antifade reagent (#P36934, Life Technologies). The samples were imaged as *Z*-stacks on a Nikon Ti-E spinning disc inverted confocal laser microscope equipped with a 60×/1.45 numerical aperture (NA) oil immersion objective and a complementary metal-oxide semiconductor camera (Photometrics). The *Z*-stacks were processed with ImageJ as follows: The plane was set to the image with the highest brightness, and the brightness/contrast was reset for the whole stack. Images at the outer edge of the *Z*-stack were discarded when out of focus, while the remaining stack always contained the same number of images for all samples. Subsequently, a maximum intensity projection was created, and an unsharp mask (radius, 1.0 pixels; mask weight, 0.60 pixels) was applied.

Cold shock treatment of U-2 OS cells

To depolymerize the microtubule network, U-2 OS cells seeded on 12 mm round coverslips and transduced with either GFP or TUBB4A-GFP variants 48 hours before the cold shock treatment were placed on ice and incubated for 5 and 20 min, respectively. At the desired time point, the cells were fixed with ice-cold methanol for 5 min at −20°C. The fixed cells were subsequently washed three times with PBS, and immunocytochemistry was performed as described above.

Western blot of TUBB4A-GFP forms in U-2 OS cells

U-2 OS cells seeded on 24-well plates, expressing either GFP or TUBB4A-GFP variants for 48 hours, were lysed in 50 μl per well of 2.5× Laemmli buffer [50 mM dithiothreitol, 4% SDS, 160 mM tris-HCl (pH 6.8), 20% glycerol, and bromophenol blue]. The samples were denatured at 95°C for 5 min, and the proteins were separated by SDS–polyacrylamide gel electrophoresis using 10% gels and subsequently transferred onto a nitrocellulose membrane using a Bio-Rad Trans-Blot Turbo system, as per the manufacturer's instructions.

The membranes were blocked for 1 hour at room temperature (or at 4°C overnight) in 5% skimmed milk in 1× PBST (PBS containing 0.1% Tween 20). Next, the membranes were incubated for 1.5 hours at room temperature with primary antibody cocktails, consisting either of anti-GFP (1:5000 dilution; rabbit polyclonal, Torrey Pines Biolabs) and anti–α-tubulin (1:1000 dilution; 12G10, mouse monoclonal; J. Frankel, University of Iowa) antibodies or of anti-GFP and anti–β-tubulin (1:500 dilution; AXO45, mouse monoclonal) antibodies in 5% skimmed milk in 1× PBST. The membranes were washed three times with 1× PBST for 5 min while agitating, followed by incubation with a secondary antibody mix consisting of horseradish peroxidase–conjugated goat anti-rabbit and goat anti-mouse antibodies (1:10,000 dilution each; Bethyl Laboratories) in 1× PBST. Last, the membranes were washed three times as above. The chemiluminescence signal was revealed using the Clarity Western ECL Substrate (Bio-Rad) solution and detected in a Fusion FX imaging system (VILBER).

Lentiviral particle production for oligodendrocytes

Lentiviral particles were produced according to previously published protocols (*50*). In short, 1 day before transfection, 1.5×10^6 HEK293T cells [American Type Culture Collection (ATCC)] were plated on 100-mm dishes (Corning) in DMEM (PAA Laboratories) supplemented with 10% (v/v) fetal bovine serum (FBS) (PAA Laboratories) and 1× penicillin-streptomycin (PAA Laboratories). The transfection mix consisted of 300 μl of Opti-MEM (Thermo Fisher Scientific), 2.5 μg of transfer vector (pER4; Novartis), 2.5 μg of pCMV-ΔR8.2 (Addgene), 0.3 μg of pCMV-VSV-G (Addgene), and 20 μl of Fugene HD (Promega). Per construct, four dishes were prepared. One day later, the medium was changed. The next day, the supernatant was collected and filtered (0.45-μm pore size; Merck), and the viral particles were enriched using ultracentrifugation (Beckman) at ~140,000*g*. The pellet was resuspended in 150 μl of Opti-MEM, aliquoted, and stored at −80°C. For each experiment, the needed lentiviral particles were produced in batches to reduce intraexperimental deviations. Each batch was tested for comparable overexpression efficiencies, and the required transduction volumes were determined.

Mouse oligodendrocyte preparation

Primary murine oligodendrocytes were isolated, proliferated, and differentiated as described before (*51*–*53*), except that solely the number of vital cells was considered for all cell-based calculations. Tissue collection was authorized by the local animal ethics committee (Ministerium für Energiewende, Landwirtschaft, Umwelt, Natur und Digitalisierung, Kiel, Germany). Mice were kept at constant temperature (22°C) on a 12-hour light/dark cycle and were provided with standard laboratory chow (2.98 kcal/g; Altromin, Hannover, Germany) and water ad libitum. In short, neonatal mice (P5 to P7 WT C57BL/6N; Charles River Laboratories) were euthanized using decapitation. The collected cortices were mechanoenzymatically dissociated using scalpel blades (Feather) and pipetting in a papain solution (Worthington). After a cell-bead hybridization step, $O4^+$ cells were sorted by magnetic cell separation (Miltenyi Biotech, Bergisch Gladbach, Germany). Last, 100 μl of cell suspension (~1.25×10^6 vital cells/ml) was plated dropwise in a chessboard-like manner onto poly-D-lysine/laminin-coated (Merck) 27-mm glass-bottom dishes (Thermo Fisher Scientific, Waltham, Massachusetts, USA). The dropwise plating ensured high local cell densities, improving cell viability and providing sufficient cells per experiment. After cell attachment, the dishes were filled with proliferation medium, supplemented with lentiviral particles. One day later, the medium was replaced by differentiation medium. Three days later, microtubule dynamics and microtubule incorporation were investigated.

Live-cell imaging of oligodendrocytes

All live-cell images were taken using an LSM710 laser confocal microscope (Zeiss) with a Plan-Neofluar 40×/1.3 NA oil immersion objective (Zeiss). To ensure oligodendrocytic identity, live O4 staining was applied before (*54*) each investigation. The integration of GFP-tagged TUBB4A forms into the microtubule lattice was determined using the colocalization of SiR-tubulin–stained microtubules. For this, oligodendrocytes were treated with 100 nM SiR-tubulin (Spirochrome) and 10 μM verapamil (Spirochrome) 30 min before image acquisition in the differentiation medium.

Microtubule dynamics were investigated as described (*20*). Briefly, each cell was recorded for 1 min with a frequency of 1 Hz. Each time series was processed using ImageJ to enhance the signal-to-noise ratio as follows: Bleach Corrected (exponential fit), Gaussian Blur (σ, 0.65 pixels), Unsharp Mask (radius, 1.5 pixels; mask weight, 0.60 pixels), and Multi Kymograph/walking average (two frames). The EB3-GFP comets were tracked using u-track (2.2.0) (*55*, *56*), and regions of interest (soma and processes) were manually set. The analysis pipeline was as follows: Microtubule plus-ends, detection (comet detection), tracking, and track analysis (microtubule dynamics classification) were applied by default settings. However, if necessary, then the low- and high-pass Gaussian SDs (LP and HP) and watershed segmentation parameters [minimum threshold (MT); threshold step size (TSS)] for comet detection were gradually increased to minimize nonspecific skipping of comet trajectories (at the cost of lower EB3-GFP comet number detection). This artificial jumping can lead to incorrectly longer and faster trajectories and should thus be reduced to a minimum. Typical adjusted parameter settings ranged between 1/4:3/1, 2/4:4/2, and 3/5:5/3 (LP/HP:MT/TSS). Mean values per cell were plotted as boxplots and tested using one-way analysis of variance (ANOVA) and corrected for multiple comparisons via Tukey test (GraphPad Prism, version 6.01).

Sholl analysis

The arborization of oligodendrocytes was assessed using an ImageJ plugin (Sholl Analysis 4.0.3) (*57*). For this purpose, one tile scan (~950 μm by 960 μm) was performed for each biological replicate. Only GFP^+ and $O4^+$ cells were used for further analysis. Each double-positive cell was cut out of the tile scan (depending on morphology of ~150 μm by 150 μm) and stored separately, and a binary mask was created on the basis of the O4 staining. Adjacent cells/protrusions were manually removed from the image. The Sholl analysis was started from the somatic center (step size, 2 μm), with the first ring approximately 10 μm distant from the center. Data extraction and visualization were performed using Jupyter notebook (version 6.0.1) and Excel (Microsoft Corporation, version 2013).

Whole-cell lysate preparation of HEK293T cells

Whole-cell lysates were prepared as described recently (*58*). In detail, HEK293T cells (ATCC) were maintained in DMEM (Life Technologies) supplemented with 10% (v/v) FBS (Sigma-Aldrich) and 1× penicillin-streptomycin (Life Technologies). Transfection with TUBB4A-expressing plasmids was performed as described before (*59*). Briefly, the day before the transfection, 2×10^6 cells were plated per 60-mm dish (Corning). Per construct, five dishes were prepared.

The next day, when the cells were ~80% confluent, the following transfection mix was applied per dish: 10 μl of JetPEI (Polyplus) and 5 μg of plasmid, filled with FBS-free DMEM up to a total volume of 500 μl. Two days later, the cells were detached by pipetting with ice-cold 1× PBS, collected in 50 ml of Falcon tubes, and pelleted for 10 min at 4°C and 453*g*. Next, the medium was removed, and the pellet was resuspended in 150 to 180 μl of ice-cold Brinkley Renaturing Buffer 80 (BRB80) buffer [80 mM K-Pipes (pH 6.8), 1 mM EGTA, and 1 mM $MgCl_2$] supplemented with 0.05% Triton X-100 and 1× protease inhibitor. During an incubation period of 10 min on ice, the samples were mixed twice by vigorous pipetting (without bubble formation). Subsequently, the lysate was transferred into 1.5-ml Beckman ultracentrifuge tubes followed by three times pulse sonication using a 6.5-mm probe (Branson) (output control, 1; duty cycle, 10%) and ultracentrifuged (Beckman TLA 55 rotor, Beckman Coulter optima MAX-XP) for 25 min at 4°C and 33,800*g*. The supernatant was aliquoted in 10-μl volumes, snap-frozen in liquid nitrogen, and stored at −80°C. For every experiment, lysates were produced in batches to reduce intraexperimental deviations. The batches were first checked under a fluorescence microscope and discarded if the samples' EB3-GFP expression levels were not uniform.

Protein quantification for TIRF assays

To maintain similar assay conditions, we measured the total protein concentration of all lysates after each preparation as recently described (*58*). Because of the highly controlled tubulin expression levels in cells [~3% of the total protein in cultured cells is tubulin (*60*)], the assessed and equalized total protein concentrations assured reproducible tubulin content in all assays. Using bicinchoninic acid (BCA) protein assay (Thermo Fisher Scientific), according to the manufacturer's instructions, the total protein amount was determined by mixing lysates with freshly prepared BCA reagent (sample/reagent: 1/8). The mixture was incubated for 30 min at 37°C, and the absorbance was measured at 562 nm with a microplate reader ($TriStar^2$ LB 942) using MikroWin 2010 software. The absorbance values of the standard bovine serum albumin dilution series were plotted and fitted to a linear equation to give the total protein concentration (*61*). Representatively, for one batch, we assessed the EB3-GFP concentration in the lysates using immunoblot. For this purpose, a standard dilution series of purified GFP (of known concentration) and the lysates (the same total protein amount was loaded; each lysate was adjusted beforehand to 4 μg/μl total protein concentration) were examined (fig. S4B). The immunoblot was carried out, as described above, except for the anti-GFP antibody dilution (1:2500; rabbit polyclonal, Torrey Pines Biolabs). The average EB3-GFP concentration in this batch was 1.8 μM (±0.12 μM). Because of the complete T2A self-cleavage, the TUBB4A concentration was assumed to be equimolar present in the lysates (fig. S4).

TIRF chamber preparation

The preparation of the TIRF chambers was described recently (*58*). For this, an adapted protocol was used to fabricate microfluidic chambers from (*62*, *63*) using 24 mm by 60 mm glass slides (Thermo Fisher Scientific) and 22 mm by 22 mm coverslips (VWR; thickness no. 1.5). The glassware was cleaned beforehand using ultrasonic baths. In short, the slides and coverslips were each placed into 500-ml bottles and filled consecutively with pure acetone. To avoid sticking together, the glassware was wiped with Kimtech paper and placed into the bottles one by one. Next, the bottles were put in an ultrasonic bath (Diagenode Bioruptor standard sonicator) and sonicated for 15 min at room temperature. Subsequently, the acetone was discarded, and the bottles were washed with ultrapure water. Sonication was repeated with ultrapure water and absolute ethanol, followed each by washing with ultrapure water. Last, the glassware was stored in absolute ethanol. For the microfluidic chamber assembly, each glassware was separately flamed and placed onto Kimtech paper. Subsequently, five long (~2 mm by 28 mm) pieces of double-sided adhesive tape (Tesa) were pressed with the backside of forceps onto a glass slide. The protective sheet was peeled off with forceps, and a coverslip was carefully pressed onto them. The resulting four reaction channels had a volume of ~6 to 8 μl each.

GMPCPP seed production

GMPCPP-MT seeds were made in 60 μl of BRB80 buffer consisting of 20 μM total tubulin [~85% unlabeled pig brain tubulin (*64*) and ~15% rhodamine-labeled porcine brain tubulin (Cytoskeleton Inc.)]; see (*58*). First, insoluble components were removed by centrifugation (98,400*g*, 4°C, 30 min). Then, the supernatant (soluble tubulin fraction) was transferred to a new tube, and GMPCPP (final 0.5 mM; Jena Biosciences) was added and incubated on ice for 5 min, followed by incubation at 37°C for 1 hour. The polymerized GMPCPP-MTs were pelleted at 37°C, 20,000*g* for 10 min and washed with warm BRB80 buffer at 37°C, 20,000*g* for 3 min. Last, the GMPCPP-MT pellet was resuspended in 75 μl of warm BRB80 buffer containing 10% (v/v) glycerol, aliquoted (2.5 μl), snap-frozen in liquid nitrogen, and stored at −80°C.

TIRF microscopy

The TIRF assays were performed as described here (*58*). To reduce unspecific binding, microfluidic chambers were blocked for 5 min with β-casein (50 μg/ml in BRB80; Sigma-Aldrich). To ensure growth of the MTs along the glass surface, the chambers were subsequently coated with 0.75 μM truncated mouse kinesin-1 KIF5B mutant (*65*) for 5 min. The purification of this $6His\text{-}mKIF5B\_N555^{Thr92Asn}$ form was described in (*66*). GMPCPP-MT seeds were resuspended in warm BRB80 and administered into the chambers. After 5 min, nonattached seeds were flushed out using warm BRB80. The density of the seeds was immediately verified under the TIRF microscope. During the microfluidic chamber preparation, the whole-cell lysates were first adjusted with cold BRB80 to 3 μg/μl and stored on ice. Less diluted samples (e.g., 8 μl/μg) resulted in too rapid (incompatible with the used recording rate) and seed-independent microtubule growth. After the cell lysates were flushed into the chambers, the glass slide was transferred to the TIRF microscope and was immediately imaged. The whole-cell lysate studies were carried out with a Nikon Ti-E azimuthal TIRF using an iLas-2 system (Gataca Systems) on an inverted microscope with a 100× TIRF/1.49 NA oil immersion objective with Nikon Perfect Focus System. The image series (68.1 μm by 68.1 μm) were recorded using an Evolve electron-multiplying charged-coupled device camera (Photometrics) and controlled with MetaMorph software. Each experiment was monitored for 400 s with a frame interval of 2.17 s.

The videos were processed using ImageJ (*67*). Briefly, *xy* drifts were eliminated with the StackReg plugin (*68*), followed by background subtraction (rolling ball radius, 20 pixels). The signal-to-noise ratio of kymographs was improved with the Gaussian blur (σ, 0.7 pixels) and the Unsharp Mask (σ, 2 pixels; mask weight, 0.7 pixels) functions, respectively. Using the Simple Neurite Tracer plugin (*69*), the EB3-GFP tracks were traced, resulting in path lengths and the corresponding start and end points as spatiotemporal *xy* coordinates. These coordinates were used to calculate the velocities, run times, run lengths, and the number of growth events. The growth of a microtubule (and the resulting velocity, run length, and run time) was analyzed in individual steps between pause events and not as the entire growth course of a kymograph. The distribution of the raw data was visualized as rain cloud plots (*70*). The data distribution was tested using one-way ANOVA and corrected for multiple testing (Dunnett); the adjusted *P* values for significant differences are shown (GraphPad Prism version 6.01). For the presentation of the temporal change of microtubule dynamics, all measured events per frame were summed up and divided by the number of measured microtubules. Data extraction and visualization were performed using Jupyter notebook (version 6.0.1) and Excel (Microsoft Corporation, version 2013).

Molecular modeling

A suitable template structure had to be found because no three-dimensional structure was available for a TUBA1A/TUBB4A heterodimer simulation. Therefore, we searched for an unmutated, drug-free, and curved template crystal structure, which should be highly similar to a TUBA1A/TUBB4A heterodimer (UniProt IDs: Q71U36/P04350). Homology detection was conducted with HHpred (*71*) using the PDB_mmCIF70 database (November 2017). We chose the $\alpha_1\beta_1$ heterodimer (TUBA1B/TUB2B) of a tubulin-stathmin complex [PDB code: 4IHJ (*29*)] given that it had the highest homology for both tubulin subunits and met all previously mentioned conditions.

The following steps were performed using the Schrödinger Suite molecular modeling package (*72*). In analogy to the HHPred alignment, the WT homology model of TUBA1A/TUBB4A heterodimer [p.M1-V437 (TUBA1A) and p.M1-A428 (TUBB4A)] was built knowledge-based using Prime (*73*, *74*), including heterodimer-associated Mg^{2+} (E- and N-site) and guanosine diphosphate (E-site) and guanosine triphosphate (N-site). Nontemplate loops were refined with the variable-dielectric surface area-based generalized Born (VSGB) solvation model using the Prime Loop Refinement. The overall stability of the model was verified using a Ramachandram plot. Steric conflicts, bond lengths, angle deviations, etc. were fixed using the Protein Preparation Wizard (*75*). The obtained WT homology model was used to introduce each of the p.R2G, p.R2W, and p.D249N mutations into the β subunit, generating three new mutant heterodimers. The corresponding amino acid side chains were generated, using the most sterically favorable rotamers. Last, all four respective heterodimers were energy-minimized using the OPLS3e force field (*76*) to a gradient of 0.05 by Prime.

Molecular simulation

The following molecular simulations were performed using Desmond Schrödinger Release 2019-1 (*77*). For each minimized structure, an orthorhombic simulation box with periodic boundary conditions was calculated using the buffer method, in which the heterodimer has at least 15-Å distance to all sides of the box (total size of ~132 Å by 92 Å by 90 Å). The system was equilibrated with TIP3P water molecules and neutralized with 150 mM NaCl. Before the simulation, the system was relaxed. Each heterodimer was simulated three times for 1 μs, with a recording interval of 300 ps under constant particle number, pressure, and temperature (NPT) conditions using Nose-Hoover chain temperature coupling and Martyna-Tobias-Klein isotropic scaling at 300 K and 1.01325 bar, respectively.

After the simulations, the RMSD and RMSF were analyzed using an in-built simulation interaction diagram of Desmond Schrödinger Release 2019-1. The PCA was performed with an in-build script (trj_essential_dynamics.py) to investigate the most prevalent motions during the simulations. For the intradimer angle determination, a previously published script was applied (*30*). For this, each subunit of a simulated heterodimer was aligned to a reference structure (PDB ID: 3J6E), and the curvature and twisting movements relative to the reference structure were measured. As described earlier (*30*, *78*), the following domains were used for alignment: Cα for α-tubulins: p.M1 to p.I30, p.V62 to p.D205, and p.A383 to p.E433; Cα for β-tubulins: p.M1 to p.D203 and p.T372 to p.D427. Clockwise twisting motions (viewed from the microtubule plus-end) were defined as positive values and anticlockwise twists as negative values (*30*).

Intradimer H-bond and salt bridge interactions were analyzed with a customized Python script (trj_analyze_pp.py; Schrödinger). The script took into account the periodic boundary conditions. For the hydrogen bonds, the following rules were applied: minimum acceptor angle of 90°, minimum donor angle of 120°, and maximum distance of 2.5 Å; for the salt bridges, a maximum distance of 4 Å was considered. The frequency was defined as interaction occurrence/frame count. The interactions were not differentiated in donor and acceptor directions. The salt bridge clusters consisted of the following interactions (TUBB4A-TUBA1A): p.E45-p.R79 and p.R46-p.D76 (frontal); p.R251-p.E97, p.R251-p.D98, p.K252-p.E71, and p.K252-p.D98 (center); and p.D427-p.K401 (back). The hydrogen bond clusters enclosed these interactions (TUBB4A-TUBA1A): p.M1-p.K96, p.M1-p.D98, p.R/G/W2-p.D98, and p.R/G/W2-p.K96 (N terminus) and p.D/N249-p.E71, p.D/N249-p.D98, p.R251-p.E97, p.R251-p.D98, p.K252-p.E71, p.K252-p.D98, and p.252K-p.N101 (center). Data extraction and visualization were performed using Jupyter notebook (version 6.0.1) and Excel (Microsoft Corporation, version 2013).

SUPPLEMENTARY MATERIALS

Supplementary material for this article is available at https://science.org/doi/10.1126/sciadv.abj9229

View/request a protocol for this paper from *Bio-protocol*.

REFERENCES AND NOTES

1. E. L. Heinzen, K. J. Swoboda, Y. Hitomi, F. Gurrieri, S. Nicole, B. de Vries, F. D. Tiziano, B. Fontaine, N. M. Walley, S. Heavin, E. Panagiotakaki; European Alternating Hemiplegia of Childhood (AHC) Genetics Consortium; Biobanca e Registro Clinico per l'Emiplegia Alternante (I.B.AHC) Consortium; European Network for Research on Alternating Hemiplegia (ENRAH) for Small and Medium-sized Enterpriese (SMEs) Consortium, S. Fiori, E. Abiusi, L. D. Pietro, M. T. Sweney, T. M. Newcomb, L. Viollet, C. Huff, L. B. Jorde, S. P. Reyna, K. J. Murphy, K. V. Shianna, C. E. Gumbs, L. Little, K. Silver, L. J. Ptáček, J. Haan, M. D. Ferrari, A. M. Bye, G. K. Herkes, C. M. Whitelaw, D. Webb, B. J. Lynch, P. Uldall, M. D. King, I. E. Scheffer, G. Neri, A. Arzimanoglou, A. M. J. M. van den Maagdenberg, S. M. Sisodiya, M. A. Mikati, D. B. Goldstein, De novo mutations in ATP1A3 cause alternating hemiplegia of childhood. *Nat Genet.* **44**, 1030–1034 (2012).
2. H. Rosewich, H. Thiele, A. Ohlenbusch, U. Maschke, J. Altmüller, P. Frommolt, B. Zirn, F. Ebinger, H. Siemes, P. Nürnberg, K. Brockmann, J. Gärtner, Heterozygous de-novo mutations in ATP1A3 in patients with alternating hemiplegia of childhood: A whole-exome sequencing gene-identification study. *Lancet Neurol.* **11**, 764–773 (2012).
3. P. de Carvalho Aguiar, K. J. Sweadner, J. T. Penniston, J. Zaremba, L. Liu, M. Caton, G. Linazasoro, M. Borg, M. A. J. Tijssen, S. B. Bressman, W. B. Dobyns, A. Brashear, L. J. Ozelius, Mutations in the Na+/K+ -ATPase alpha3 gene ATP1A3 are associated with rapid-onset dystonia parkinsonism. *Neuron* **43**, 169–175 (2004).
4. M. K. Demos, C. D. van Karnebeek, C. J. Ross, S. Adam, Y. Shen, S. H. Zhan, C. Shyr, G. Horvath, M. Suri, A. Fryer, S. J. Jones, J. M. Friedman; FORGE Canada Consortium, A novel recurrent mutation in ATP1A3 causes CAPOS syndrome. *Orphanet J Rare Dis.* **9**, 15 (2014).
5. L. Prange, M. Pratt, K. Herman, R. Schiffmann, D. M. Mueller, M. McLean, M. M. Mendez, N. Walley, E. L. Heinzen, D. Goldstein, V. Shashi, A. Hunanyan, V. Pagadala, M. A. Mikati,

D-DEMØ, a distinct phenotype caused by ATP1A3 mutations. *Neurol Genet.* **6**, e466 (2020).

6. C. Janke, M. M. Magiera, The tubulin code and its role in controlling microtubule properties and functions. *Nat. Rev. Mol. Cell Biol.* **21**, 307–326 (2020).
7. G. J. Brouhard, L. M. Rice, Microtubule dynamics: An interplay of biochemistry and mechanics. *Nat. Rev. Mol. Cell Biol.* **19**, 451–463 (2018).
8. A. Roll-Mecak, The tubulin code in microtubule dynamics and information encoding. *Dev. Cell* **54**, 7–20 (2020).
9. T. Mitchison, M. Kirschner, Dynamic instability of microtubule growth. *Nature* **312**, 237–242 (1984).
10. J. Hersheson, N. E. Mencacci, M. Davis, N. MacDonald, D. Trabzuni, M. Ryten, A. Pittman, R. Paudel, E. Kara, K. Fawcett, V. Plagnol, K. P. Bhatia, A. J. Medlar, H. C. Stanescu, J. Hardy, R. Kleta, N. W. Wood, H. Houlden, Mutations in the autoregulatory domain of β-tubulin 4a cause hereditary dystonia. *Ann. Neurol.* **73**, 546–553 (2013).
11. K. Lohmann, R. A. Wilcox, S. Winkler, A. Ramirez, A. Rakovic, J.-S. Park, B. Arns, T. Lohnau, J. Groen, M. Kasten, N. Brüggemann, J. Hagenah, A. Schmidt, F. J. Kaiser, K. R. Kumar, K. Zschiedrich, D. Alvarez-Fischer, E. Altenmüller, A. Ferbert, A. E. Lang, A. Münchau, V. Kostic, K. Simonyan, M. Agzarian, L. J. Ozelius, A. P. M. Langeveld, C. M. Sue, M. A. J. Tijssen, C. Klein, Whispering dysphonia (DYT4 dystonia) is caused by a mutation in the TUBB4 gene. *Ann. Neurol.* **73**, 537–545 (2013).
12. A. Pizzino, T. M. Pierson, Y. Guo, G. Helman, S. Fortini, K. Guerrero, S. Saitta, J. L. P. Murphy, Q. Padiath, Y. Xie, H. Hakonarson, X. Xu, T. Funari, M. Fox, R. J. Taft, M. S. van der Knaap, G. Bernard, R. Schiffmann, C. Simons, A. Vanderver, TUBB4A de novo mutations cause isolated hypomyelination. *Neurology* **83**, 898–902 (2014).
13. C. Simons, N. I. Wolf, N. McNeil, L. Caldovic, J. M. Devaney, A. Takanohashi, J. Crawford, K. Ru, S. M. Grimmond, D. Miller, D. Tonduti, J. L. Schmidt, R. S. Chudnow, R. van Coster, L. Lagae, J. Kisler, J. Sperner, M. S. van der Knaap, R. Schiffmann, R. J. Taft, A. Vanderver, A de novo mutation in the β-tubulin gene TUBB4A results in the leukoencephalopathy hypomyelination with atrophy of the basal ganglia and cerebellum. *Am. J. Hum. Genet.* **92**, 767–773 (2013).
14. E. M. Hamilton, E. Polder, A. Vanderver, S. Naidu, R. Schiffmann, K. Fisher, A. B. Raguž, L. Blumkin; H-ABC Research Group, C. G. M. van Berkel, Q. Waisfisz, C. Simons, R. J. Taft, T. E. M. Abbink, N. I. Wolf, M. S. van der Knaap, Hypomyelination with atrophy of the basal ganglia and cerebellum: Further delineation of the phenotype and genotype-phenotype correlation. *Brain* **137**, 1921–1930 (2014).
15. S. Miyatake, H. Osaka, M. Shiina, M. Sasaki, J.-I. Takanashi, K. Haginoya, T. Wada, M. Morimoto, N. Ando, Y. Ikuta, M. Nakashima, Y. Tsurusaki, N. Miyake, K. Ogata, N. Matsumoto, H. Saitsu, Expanding the phenotypic spectrum of TUBB4A-associated hypomyelinating leukoencephalopathies. *Neurology* **82**, 2230–2237 (2014).
16. N. Parker, Hereditary whispering dysphonia. *J. Neurol. Neurosurg. Psychiatry* **48**, 218–224 (1985).
17. R. A. Wilcox, S. Winkler, K. Lohmann, C. Klein, Whispering dysphonia in an Australian family (DYT4): A clinical and genetic reappraisal. *Mov. Disord.* **26**, 2404–2408 (2011).
18. M. S. van der Knaap, S. Naidu, P. J. W. Pouwels, S. Bonavita, R. van Coster, L. Lagae, J. Sperner, R. Surtees, R. Schiffmann, J. Valk, New syndrome characterized by hypomyelination with atrophy of the basal ganglia and cerebellum. *AJNR Am. J. Neuroradiol.* **23**, 1466–1474 (2002).
19. J. Curiel, G. Rodríguez Bey, A. Takanohashi, M. Bugiani, X. Fu, N. I. Wolf, B. Nmezi, R. Schiffmann, M. Bugaighis, T. Pierson, G. Helman, C. Simons, M. S. van der Knaap, J. Liu, Q. Padiath, A. Vanderver, TUBB4A mutations result in specific neuronal and oligodendrocytic defects that closely match clinically distinct phenotypes. *Hum. Mol. Genet.* **26**, 4506–4518 (2017).
20. F. Vulinovic, V. Krajka, T. J. Hausrat, P. Seibler, D. Alvarez-Fischer, H. Madoev, J.-S. Park, K. R. Kumar, C. M. Sue, K. Lohmann, M. Kneussel, C. Klein, A. Rakovic, Motor protein binding and mitochondrial transport are altered by pathogenic TUBB4A variants. *Hum. Mutat.* **39**, 1901–1915 (2018).
21. N. Watanabe, M. Itakaoka, Y. Seki, T. Morimoto, K. Homma, Y. Miyamoto, J. Yamauchi, Dystonia-4 (DYT4)-associated TUBB4A mutants exhibit disorganized microtubule networks and inhibit neuronal process growth. *Biochem. Biophys. Res. Commun.* **495**, 346–352 (2018).
22. I. D. Duncan, M. Bugiani, A. B. Radcliff, J. J. Moran, C. Lopez-Anido, P. Duong, B. K. August, N. I. Wolf, M. S. van der Knaap, J. Svaren, A mutation in the Tubb4a gene leads to microtubule accumulation with hypomyelination and demyelination. *Ann. Neurol.* **81**, 690–702 (2017).
23. S. Sase, A. A. Almad, C. A. Boecker, P. Guedes-Dias, J. J. Li, A. Takanohashi, A. Patel, T. McCaffrey, H. Patel, D. Sirdeshpande, J. Curiel, J. Shih-Hwa Liu, Q. Padiath, E. L. Holzbaur, S. S. Scherer, A. Vanderver, TUBB4A mutations result in both glial and neuronal degeneration in an H-ABC leukodystrophy mouse model. *Elife* **9**, e52986 (2020).
24. J. F. Bally, S. Camargos, C. Oliveira Dos Santos, D. S. Kern, T. Lee, F. Pereira da Silva-Junior, R. D. Puga, F. Cardoso, E. R. Barbosa, R. Yadav, L. J. Ozelius, P. de Carvalho Aguiar, A. E. Lang, DYT-TUBB4A (DYT4 dystonia): New clinical and genetic observations. *Neurology* **96**, e1887–e1897 (2021).
25. T. J. Yen, P. S. Machlin, D. W. Cleveland, Autoregulated instability of β-tubulin mRNAs by recognition of the nascent amino terminus of βtubulin. *Nature* **334**, 580–585 (1988).
26. Y. Zhang, K. Chen, S. A. Sloan, M. L. Bennett, A. R. Scholze, S. O'Keeffe, H. P. Phatnani, P. Guarnieri, C. Caneda, N. Ruderisch, S. Deng, S. A. Liddelow, C. Zhang, R. Daneman, T. Maniatis, B. A. Barres, J. Q. Wu, An RNA-sequencing transcriptome and splicing database of glia, neurons, and vascular cells of the cerebral cortex. *J. Neurosci.* **34**, 11929–11947 (2014).
27. S. Marques, A. Zeisel, S. Codeluppi, D. van Bruggen, A. Mendanha Falcão, L. Xiao, H. Li, M. Häring, H. Hochgerner, R. A. Romanov, D. Gyllborg, A. Muñoz Manchado, G. La Manno, P. Lönnerberg, E. M. Floriddia, F. Rezayee, P. Ernfors, E. Arenas, J. Hjerling-Leffler, T. Harkany, W. D. Richardson, S. Linnarsson, G. Castelo-Branco, Oligodendrocyte heterogeneity in the mouse juvenile and adult central nervous system. *Science* **352**, 1326–1329 (2016).
28. Y. Zhang, S. A. Sloan, L. E. Clarke, C. Caneda, C. A. Plaza, P. D. Blumenthal, H. Vogel, G. K. Steinberg, M. S. B. Edwards, G. Li, J. A. Duncan, S. H. Cheshier, L. M. Shuer, E. F. Chang, G. A. Grant, M. G. H. Gephart, B. A. Barres, Purification and characterization of progenitor and mature human astrocytes reveals transcriptional and functional differences with mouse. *Neuron* **89**, 37–53 (2016).
29. A. E. Prota, M. M. Magiera, M. Kuijpers, K. Bargsten, D. Frey, M. Wieser, R. Jaussi, C. C. Hoogenraad, R. A. Kammerer, C. Janke, M. O. Steinmetz, Structural basis of tubulin tyrosination by tubulin tyrosine ligase. *J. Cell Biol.* **200**, 259–270 (2013).
30. V. A. Fedorov, P. S. Orekhov, E. G. Kholina, A. A. Zhmurov, F. I. Ataullakhanov, I. B. Kovalenko, N. B. Gudimchuk, Mechanical properties of tubulin intra- and inter-dimer interfaces and their implications for microtubule dynamic instability. *PLoS Comput. Biol.* **15**, e1007327 (2019).
31. T. D. Cushion, A. R. Paciorkowski, D. T. Pilz, J. G. L. Mullins, L. E. Seltzer, R. W. Marion, E. Tuttle, D. Ghoneim, S. L. Christian, S.-K. Chung, M. I. Rees, W. B. Dobyns, De novo mutations in the beta-tubulin gene TUBB2A cause simplified gyral patterning and infantile-onset epilepsy. *Am. J. Hum. Genet.* **94**, 634–641 (2014).
32. S.-C. Ti, M. C. Pamula, S. C. Howes, C. Duellberg, N. I. Cade, R. E. Kleiner, S. Forth, T. Surrey, E. Nogales, T. M. Kapoor, Mutations in human tubulin proximal to the kinesin-binding site alter dynamic instability at microtubule plus- and minus-ends. *Dev. Cell* **37**, 72–84 (2016).
33. Z. Lin, I. Gasic, V. Chandrasekaran, N. Peters, S. Shao, T. J. Mitchison, R. S. Hegde, TTC5 mediates autoregulation of tubulin via mRNA degradation. *Science* **367**, 100–104 (2020).
34. C. Ferreira, A. Poretti, J. Cohen, A. Hamosh, S. Naidu, Novel TUBB4A mutations and expansion of the neuroimaging phenotype of hypomyelination with atrophy of the basal ganglia and cerebellum (H-ABC). *Am. J. Med. Genet. A* **164A**, 1802–1807 (2014).
35. D. Carvalho, S. Santos, B. Martins, F. P. Marques, TUBB4A novel mutation reinforces the genotype-phenotype correlation of hypomyelination with atrophy of the basal ganglia and cerebellum. *Brain* **138**, e327 (2015).
36. X. H. Jaglin, K. Poirier, Y. Saillour, E. Buhler, G. Tian, N. Bahi-Buisson, C. Fallet-Bianco, F. Phan-Dinh-Tuy, X. P. Kong, P. Bomont, L. Castelnau-Ptakhine, S. Odent, P. Loget, M. Kossorotoff, I. Snoeck, G. Plessis, P. Parent, C. Beldjord, C. Cardoso, A. Represa, J. Flint, D. A. Keays, N. J. Cowan, J. Chelly, Mutations in the beta-tubulin gene TUBB2B result in asymmetrical polymicrogyria. *Nat. Genet.* **41**, 746–752 (2009).
37. M. A. Tischfield, H. N. Baris, C. Wu, G. Rudolph, L. Van Maldergem, W. He, W.-M. Chan, C. Andrews, J. L. Demer, R. L. Robertson, D. A. Mackey, J. B. Ruddle, T. D. Bird, I. Gottlob, C. Pieh, E. I. Traboulsi, S. L. Pomeroy, D. G. Hunter, J. S. Soul, A. Newlin, L. J. Sabol, E. J. Doherty, C. E. de Uzcátegui, N. de Uzcátegui, M. L. Z. Collins, E. C. Sener, B. Wabbels, H. Hellebrand, T. Meitinger, T. de Berardinis, A. Magli, C. Schiavi, M. Pastore-Trossello, F. Koc, A. M. Wong, A. V. Levin, M. T. Geraghty, M. Descartes, M. Flaherty, R. V. Jamieson, H. U. Møller, I. Meuthen, D. F. Callen, J. Kerwin, S. Lindsay, A. Meindl, M. L. Gupta, D. Pellman, E. C. Engle, Human TUBB3 mutations perturb microtubule dynamics, kinesin interactions, and axon guidance. *Cell* **140**, 74–87 (2010).
38. A. Sferra, F. Fattori, T. Rizza, E. Flex, E. Bellacchio, A. Bruselles, S. Petrini, S. Cecchetti, M. Teson, F. Restaldi, A. Ciolfi, F. M. Santorelli, G. Zanni, S. Barresi, C. Castiglioni, M. Tartaglia, E. Bertini, Defective kinesin binding of TUBB2A causes progressive spastic ataxia syndrome resembling sacsinopathy. *Hum. Mol. Genet.* **27**, 1892–1904 (2018).
39. I. Gasic, S. A. Boswell, T. J. Mitchison, Tubulin mRNA stability is sensitive to change in microtubule dynamics caused by multiple physiological and toxic cues. *PLoS Biol.* **17**, e3000225 (2019).
40. M. Knossow, V. Campanacci, L. A. Khodja, B. Gigant, The mechanism of tubulin assembly into microtubules: Insights from structural studies. *iScience* **23**, 101511 (2020).
41. L. Cao, W. Wang, Q. Jiang, C. Wang, M. Knossow, B. Gigant, The structure of apo-kinesin bound to tubulin links the nucleotide cycle to movement. *Nat. Commun.* **5**, 5364 (2014).
42. C. Zheng, M. Diaz-Cuadros, K. C. Q. Nguyen, D. H. Hall, M. Chalfie, Distinct effects of tubulin isotype mutations on neurite growth in *Caenorhabditis elegans*. *Mol. Biol. Cell* **28**, 2786–2801 (2017).

43. M. Fu, T. S. McAlear, H. Nguyen, J. A. Oses-Prieto, A. Valenzuela, R. D. Shi, J. J. Perrino, T.-T. Huang, A. L. Burlingame, S. Bechstedt, B. A. Barres, The Golgi outpost protein TPPP nucleates microtubules and is critical for myelination. *Cell* **179**, 132–146.e14 (2019).
44. X. Liang, M. Kokes, R. D. Fetter, M. D. Sallee, A. W. Moore, J. L. Feldman, K. Shen, Growth cone-localized microtubule organizing center establishes microtubule orientation in dendrites. *eLife* **9**, e56547 (2020).
45. B. Y. Lee, E.-M. Hur, A role of microtubules in oligodendrocyte differentiation. *Int. J. Mol. Sci.*. **21**, 1062 (2020).
46. D. A. Brito, C. L. Rieder, The ability to survive mitosis in the presence of microtubule poisons differs significantly between human nontransformed (RPE-1) and cancer (U2OS, HeLa) cells. *Cell Motil. Cytoskeleton* **66**, 437–447 (2009).
47. R. Marisca, T. Hoche, E. Agirre, L. J. Hoodless, W. Barkey, F. Auer, G. Castelo-Branco, T. Czopka, Functionally distinct subgroups of oligodendrocyte precursor cells integrate neural activity and execute myelin formation. *Nat. Neurosci.* **23**, 363–374 (2020).
48. J. Song, J. H. Carson, E. Barbarese, F.-Y. Li, I. D. Duncan, RNA transport in oligodendrocytes from the taiep mutant rat. *Mol. Cell. Neurosci.* **24**, 926–938 (2003).
49. M. M. Magiera, C. Janke, Investigating tubulin posttranslational modifications with specific antibodies. *Methods Cell Biol.* **115**, 247–267 (2013).
50. I.-H. Park, R. Zhao, J. A. West, A. Yabuuchi, H. Huo, T. A. Ince, P. H. Lerou, M. W. Lensch, G. Q. Daley, Reprogramming of human somatic cells to pluripotency with defined factors. *Nature* **451**, 141–146 (2008).
51. T. A. Dincman, J. E. Beare, S. S. Ohri, S. R. Whittemore, Isolation of cortical mouse oligodendrocyte precursor cells. *J. Neurosci. Methods* **209**, 219–226 (2012).
52. B. Emery, J. C. Dugas, Purification of oligodendrocyte lineage cells from mouse cortices by immunopanning. *Cold Spring Harb. Protoc.* **2013**, 854–868 (2013).
53. R. E. Flores-Obando, M. M. Freidin, C. K. Abrams, Rapid and specific immunomagnetic isolation of mouse primary oligodendrocytes. *J Vis Exp* , 57543 (2018).
54. P. Douvaras, V. Fossati, Generation and isolation of oligodendrocyte progenitor cells from human pluripotent stem cells. *Nat. Protoc.* **10**, 1143–1154 (2015).
55. K. Jaqaman, D. Loerke, M. Mettlen, H. Kuwata, S. Grinstein, S. L. Schmid, G. Danuser, Robust single-particle tracking in live-cell time-lapse sequences. *Nat. Methods* **5**, 695–702 (2008).
56. K. T. Applegate, S. Besson, A. Matov, M. H. Bagonis, K. Jaqaman, G. Danuser, plusTipTracker: Quantitative image analysis software for the measurement of microtubule dynamics. *J. Struct. Biol.* **176**, 168–184 (2011).
57. T. A. Ferreira, A. V. Blackman, J. Oyrer, S. Jayabal, A. J. Chung, A. J. Watt, P. J. Sjöström, D. J. van Meyel, Neuronal morphometry directly from bitmap images. *Nat. Methods* **11**, 982–984 (2014).
58. A. S. Jijumon, S. Bodakuntla, M. Genova, M. Bangera, V. Sackett, L. Besse, F. Maksut, V. Henriot, M. M. Magiera, M. Sirajuddin, C. Janke, Lysate-based pipeline to characterize microtubule-associated proteins uncovers unique microtubule behaviours. *Nat. Cell Biol.* 10.1038/s41556-41021-00825-41554 , (2022).
59. J. Souphron, S. Bodakuntla, A. S. Jijumon, G. Lakisic, A. M. Gautreau, C. Janke, M. M. Magiera, Purification of tubulin with controlled post-translational modifications by polymerization-depolymerization cycles. *Nat. Protoc.* **14**, 1634–1660 (2019).
60. G. Hiller, K. Weber, Radioimmunoassay for tubulin: A quantitative comparison of the tubulin content of different established tissue culture cells and tissues. *Cell* **14**, 795–804 (1978).
61. P. N. Brady, M. A. Macnaughtan, Evaluation of colorimetric assays for analyzing reductively methylated proteins: Biases and mechanistic insights. *Anal. Biochem.* **491**, 43–51 (2015).
62. C. Gell, V. Bormuth, G. J. Brouhard, D. N. Cohen, S. Diez, C. T. Friel, J. Helenius, B. Nitzsche, H. Petzold, J. Ribbe, E. Schäffer, J. H. Stear, A. Trushko, V. Varga, P. O. Widlund, M. Zanic, J. Howard, Microtubule dynamics reconstituted in vitro and imaged by single-molecule fluorescence microscopy. *Methods Cell Biol.* **95**, 221–245 (2010).
63. W. Li, T. Moriwaki, T. Tani, T. Watanabe, K. Kaibuchi, G. Goshima, Reconstitution of dynamic microtubules with Drosophila XMAP215, EB1, and Sentin. *J. Cell Biol.* **199**, 849–862 (2012).
64. M. Castoldi, A. V. Popov, Purification of brain tubulin through two cycles of polymerization–depolymerization in a high-molarity buffer. *Protein Expr. Purif.* **32**, 83–88 (2003).
65. T. Nakata, N. Hirokawa, Point mutation of adenosine triphosphate-binding motif generated rigor kinesin that selectively blocks anterograde lysosome membrane transport. *J. Cell Biol.* **131**, 1039–1053 (1995).
66. P. Dutta, A. S. Jijumon, M. Mazumder, D. Dileep, A. K. Mukhopadhyay, S. Gourinath, S. Maiti, Presence of actin binding motif in VgrG-1 toxin of Vibrio cholerae reveals the molecular mechanism of actin cross-linking. *Int. J. Biol. Macromol.* **133**, 775–785 (2019).
67. C. A. Schneider, W. S. Rasband, K. W. Eliceiri, NIH Image to ImageJ: 25 years of image analysis. *Nat. Methods* **9**, 671–675 (2012).
68. P. Thévenaz, U. E. Ruttimann, M. Unser, A pyramid approach to subpixel registration based on intensity. *IEEE Trans. Image Process.* **7**, 27–41 (1998).
69. M. H. Longair, D. A. Baker, J. D. Armstrong, Simple Neurite Tracer: Open source software for reconstruction, visualization and analysis of neuronal processes. *Bioinformatics* **27**, 2453–2454 (2011).
70. M. Allen, D. Poggiali, K. Whitaker, T. R. Marshall, R. A. Kievit, Raincloud plots: A multi-platform tool for robust data visualization. *Wellcome Open Res.* **4**, 63 (2019).
71. L. Zimmermann, A. Stephens, S.-Z. Nam, D. Rau, J. Kübler, M. Lozajic, F. Gabler, J. Söding, A. N. Lupas, V. Alva, A completely reimplemented mpi bioinformatics toolkit with a new HHpred server at its core. *J. Mol. Biol.* **430**, 2237–2243 (2018).
72. *Schrödinger Release 2019–1: Maestro, Schrödinger, LLC, New York, NY* (2019).
73. M. P. Jacobson, D. L. Pincus, C. S. Rapp, T. J. F. Day, B. Honig, D. E. Shaw, R. A. Friesner, A hierarchical approach to all-atom protein loop prediction. *Proteins* **55**, 351–367 (2004).
74. M. P. Jacobson, R. A. Friesner, Z. Xiang, B. Honig, On the role of the crystal environment in determining protein side-chain conformations. *J. Mol. Biol.* **320**, 597–608 (2002).
75. G. M. Sastry, M. Adzhigirey, T. Day, R. Annabhimoju, W. Sherman, Protein and ligand preparation: Parameters, protocols, and influence on virtual screening enrichments. *J. Comput. Aided Mol. Des.* **27**, 221–234 (2013).
76. E. Harder, W. Damm, J. Maple, C. Wu, M. Reboul, J. Y. Xiang, L. Wang, D. Lupyan, M. K. Dahlgren, J. L. Knight, J. W. Kaus, D. S. Cerutti, G. Krilov, W. L. Jorgensen, R. Abel, R. A. Friesner, OPLS3: A force field providing broad coverage of drug-like small molecules and proteins. *J Chem Theory Comput.* **12**, 281–296 (2016).
77. K. J. Bowers, D. E. Chow, H. Xu, R. O. Dror, M. P. Eastwood, B. A. Gregersen, J. L. Klepeis, I. Kolossvary, M. A. Moraes, F. D. Sacerdoti, J. K. Salmon, Y. Shan, D. E. Shaw, Scalable algorithms for molecular dynamics simulations on commodity clusters. *Proc. ACM/IEEE Conf. Supercomput.* 43 (2006).
78. A. Grafmüller, G. A. Voth, Intrinsic bending of microtubule protofilaments. *Structure* **19**, 409–417 (2011).
79. J. Aiken, G. Buscaglia, E. A. Bates, J. K. Moore, The α-tubulin gene TUBA1A in brain development: A key ingredient in the neuronal isotype blend. *J. Dev. Biol.* **5**, jdb5030008 (2017).

Acknowledgments: We thank N. Gudimchuk and V. Federov (Department of Physics, Lomonosov Moscow State University) for the PyMOL script to evaluate the heterodimer angles, V. Henriot (Institut Curie) for technical assistance during revision experiments, and members of the Klein and Janke laboratories for stimulating discussions. **Funding:** We acknowledge financial support by Land Schleswig-Holstein within the funding program Open Access Publikationsfonds, German Research Foundation grant FOR 2488 (to C.K. and A.R.), EMBO Short-Term Fellowship 8300 (to V.K.), French National Research Agency ANR-10-IDEX-0001-02 (to C.J.), French National Research Agency LabEx Cell(n)Scale ANR-11-LBX-0038 (to C.J.), French National Research Agency ANR-17-CE13-0021 (to C.J.), French National Research Agency ANR-20-CE13-0011 (to C.J.), Fondation pour la Recherche Médicale DEQ20170336756 (to C.J.), European Union's Horizon 2020 research and innovation program under the Marie Skłodowska-Curie grant agreement 675737 (to A.S.J.), Fondation pour la Recherche Médicale FDT201904008210 (to A.S.J.), Fondation pour la Recherche Médicale FDT201805005465 (to S.B.), and Institut Curie 3-i Ph.D. Program (to M.G.). **Author contributions:** Conceptualization: V.K., F.V., K.T., A.S.J., S.B., H.M.-F., S.T., C.J., C.K., and A.R. Data curation: V.K. and S.T. Formal analysis: V.K. Funding acquisition: V.K., C.J., C.K., and A.R. Investigation: V.K., F.V., M.G., and K.T. Methodology: V.K., M.G., A.S.J., S.B., H.M.-F., B.M., S.T., and A.R. Project administration: V.K., S.T., C.J., C.K., and A.R. Resources: S.T., C.J., and A.R. Software: V.K. and S.T. Supervision: V.K., S.T., C.J., C.K., and A.R. Validation: V.K., B.M., and S.T. Visualization: V.K. Writing—Original draft preparation: V.K., C.K., and A.R. Writing—Review and editing: V.K., F.V., M.G., K.T., A.S.J., S.B., H.M.-F., S.T., C.J., C.K., and A.R. **Competing interests:** C.K. serves as a medical advisor to Centogene on genetic testing reports in the fields of movement disorders and dementia, excluding Parkinson's disease, and on the scientific advisory board of Retromer Therapeutics; however, none of these sources contributed to the current project. All other authors declare that they have no competing interests. **Data and materials availability:** All data needed to evaluate the conclusions in the paper are present in the paper and/or the Supplementary Materials.

Submitted 1 July 2021
Accepted 22 January 2022
Published 11 March 2022
10.1126/sciadv.abj9229